

# **Polarization Conversion mediated by Surface Plasmon Polaritons in Extraordinary Optical Transmission through a Nanohole Array**

Romain Debroux

Thesis submitted to the Faculty of the Virginia Polytechnic Institute and State University

in partial fulfillment of the requirements for the degree of

Master of Science

Electrical Engineering

Wei Zhou, Chair

Ting-Chung Poon

Sophia E. Economou

May 3<sup>rd</sup> 2018

Blacksburg, VA

Keywords: Plasmonics, Surface Plasmon Polariton, Extraordinary Optical Transmission,  
Periodic Nanohole Array, Polarization Conversion

Copyright 2018, Romain Debroux

# Polarization Conversion mediated by Surface Plasmon Polaritons in Extraordinary Optical Transmission through a Nanohole Array

Romain Debroux

## Abstract

Since Ebbesen's seminal work in 1998<sup>1</sup> observing extraordinary optical transmission (EOT) through nanohole arrays, much research has focused on the role of surface plasmon polaritons (SPPs) in EOT<sup>2-10</sup>. While the energy and momentum conditions have become clear<sup>11-16</sup>, no consensus has been reached on the role of incident light polarization<sup>17-23</sup>. This study presents a simple model that captures Bloch-SPP excitation, including the role of polarization, in general periodic plasmonic structures. Our model predicts that under certain conditions polarization conversion should occur in EOT light transmitted through the nanohole array. We experimentally measure polarization conversion in EOT and compare the experimentally obtained results to the predictions of our model. Using numerical simulations, we tie the far field experimental results to the near field underlying physics described by our model. In using polarization conversion to provide evidence supporting our model, we also establish a novel approach to achieving polarization conversion based on SPPs instead of hole shape<sup>24-30</sup> or other techniques in literature, and present reasons why this approach to achieving polarization conversion may be better suited for applications in biomedical sensing<sup>13,14</sup> and optical elements<sup>24</sup>.

# Polarization Conversion mediated by Surface Plasmon Polaritons in Extraordinary Optical Transmission through a Nanohole Array

Romain Debroux

## General Audience Abstract

In 1998, Ebbesen et al<sup>1</sup> observed that when light is shown on a metal nanofilm perforated with nanoholes more light appears on the other side of the metal film than was incident on the nanoholes. The unexpectedly high transmission of light through the nanohole array was termed extraordinary optical transmission (EOT), and quickly found applications in diverse fields such as biomedical sensing<sup>13,14</sup>, energy harvesting<sup>12,31</sup>, and nonlinear optics<sup>12-14,24</sup>. As the importance of EOT in applications became clear, interest developed in understanding the fundamental physics involved. Over the next 20 years, researchers showed that the incident light (made up of electromagnetic fields) excites conduction electrons on the surface of the metal film<sup>11</sup>. Specifically, the light and the electrons couple to form quasiparticles known as surface plasmon polaritons (SPP) which propagate along the surfaces of the metal film. The SPPs on the back surface of the metal film then radiate free space transmitted light, which is observed as EOT. However, much of the physics involved how SPPs mediate EOT has remained unclear.

The first focus of this work is theoretical, presenting a microscopic model for SPP mediated EOT. In contrast to many groups which aim to characterize SPPs from their far field properties, our model focuses on the near field microscopic physics and presents the far field properties as a consequence of the near field physics. Since the near field cannot be probed

experimentally, we use numerical simulations to both verify our model's predictions in the near field and predict the properties that should be measured in the far field.

The second focus of this work is more applications driven. We notice that our model predicts that under certain conditions SPPs should cause a phenomenon known as polarization conversion to occur, which is when the polarization of the transmitted light is different from the polarization of the incident light. We experimentally measure the predicted polarization conversion, thereby providing substantial experimental evidence in support of our theoretical model. Our novel approach to achieving polarization conversion based on the behavior of SPPs differs substantially from the approaches in literature (usually based on hole shape<sup>24</sup>). We present the reasons why our SPP-based approach to achieving polarization conversion is more robust to fabrication imperfections than the conventional approaches, and describe how our approach could affect various applications.

## Acknowledgments

I would first like to recognize my collaborators. Aditya Garg assisted me throughout this project, particularly with running the simulations. Prof. Wei Zhou advised my work and is also responsible for leading all the experimental work. Prof. Teri Odom advised Prof. Wei Zhou on the experimental work. Without their help, this project would not have been possible.

I would like to sincerely thank my advisor, Prof. Wei Zhou for his incredible personal and academic mentorship. As a professor, he taught me key concepts in nanoscience and specifically plasmonic through coursework, and helped me appreciate the importance of having a clear qualitative picture of the system studied. As an advisor, he has challenged me to be more critical when reading recent publications, to always ask myself “what are the key results and limitations of this work, and what are the gaps the entire field may be missing”, and to work towards filling those holes by approaching research creatively. As a senior colleague, he has shared his professional experiences to help me make the best decisions about my future. As a friend, he has always been understanding of my ambitions and extremely flexible in making accommodations to help me reach them.

I’ve been blessed to have been accompanied by dedicated professors and labmates throughout my four years at Virginia Tech. Among these, Prof. Sophia Economou stands out for making me fall in love with the quantum world. My labmates – Ali, Ana, Junyeob, Nam, Aditya, Kru, and Kelly – made coming to lab enjoyable and helped me in my work. Aditya, who started this project and assisted me for nearly a year, deserves special mention. I want to thank my family for their support through this process. My roommates – John, Joe, and Cara – listened to me rehearse numerous presentations and were always supportive. Finally, I want to thank my girlfriend Stephanie for her endless love and patience.

# Table of Contents

<b>Abstract</b> .....	ii
<b>General Audience Abstract</b> .....	iii
<b>Acknowledgments</b> .....	v
<b>List of Figures</b> .....	viii
<b>List of Tables</b> .....	x
<b>Chapter 1. Introduction</b> .....	1
1.1. Extraordinary Optical Transmission (EOT).....	2
1.2. Surface Plasmon Polaritons (SPPs).....	4
1.2.1. Deriving the SPP Dispersion Relation.....	4
1.2.2. Role of Energy and Momentum in SPP Excitation on Nanohole Arrays.....	8
1.2.3. Comments on Dispersion Plots.....	11
1.2.4. Role of Polarization in SPP Excitation on Nanohole Arrays.....	13
1.3. Polarization Conversion.....	17
1.4. Scope of Project.....	18
<b>Chapter 2. Conceptual Model - Predicting EOT Polarization Conversion</b> .....	19
2.1. Conceptual Model – Single Mode Regime Coupling-in Process.....	19
2.1.1. Derivation of Optimal Polarization Angle.....	21
2.2. Conceptual Model – Single Mode Regime Coupling-out Process.....	23
2.3. Analysis of Single Mode Regime Polarization Conversion.....	24
2.4. Extending the Model to the Multi-Mode Regime.....	26
2.4.1. Standing Waves from Brillouin Zone Boundaries.....	28
2.5. Assumptions.....	30
2.6. Regimes of Validity.....	31
2.7. Role of Each Variable.....	33
<b>Chapter 3. Experimental Results – Observing EOT Polarization Conversion</b> .....	36
3.1. Motivation for Experiments.....	36
3.1.1. Importance of Azimuthal Angle $\phi$ in Achieving Polarization Conversion.....	36
3.2. Experimental Set-Up.....	37
3.3. $\phi = 0^\circ$ Experiment.....	38
3.4. $\phi = 22^\circ$ Experiment.....	40
3.5. Conclusions.....	42

<b>Chapter 4. Numerical Results – Analyzing EOT Polarization Conversion</b> .....	44
4.1. Numerical Set-up .....	44
4.2. Reproducing Experimental Results.....	46
4.2.1. Simulating $\phi = 0^\circ$ Experiment.....	46
4.2.2. Simulating $\phi = 22^\circ$ Experiment.....	48
4.3. Role of Incident Light Polarization.....	50
4.4. Role of Angle of Incidence .....	53
4.5. Coupling between Bloch-SPPs on Front and Back Surfaces of Nanohole Array .....	55
4.6. Analysis of Multi-Mode Regime .....	56
4.7. Limitations of Simulations.....	58
<b>Chapter 5. Conclusions and Outlook</b> .....	60
5.1. Key Insights .....	60
5.2. Potential Applications.....	61
5.3. Future Work.....	63
<b>References</b> .....	65
<b>Appendix A. Matlab and Lumerical FDTD Scripts</b> .....	71

## List of Figures

Figure 1. Transmission spectrum through nanohole array showing original observation of EOT. Ebbesen, T., et al., "Extraordinary optical transmission through sub-wavelength hole arrays", Letters to Nature (1998) 667-669. Used under fair use, 2018. ....	3
Figure 2. Schematic of SPP excitation. Lee, B. et al., "The use of plasmonics in light beaming and focusing", Progress in Quantum Electronics (2010) 47-87. Used under fair use, 2018. ....	8
Figure 3. SPP dispersion relation. Genet, G. and Ebbesen, T., "Light in tiny holes", Nature (2007). Used under fair use, 2018.....	9
Figure 4. Geometry involved in SPP excitation.....	10
Figure 5. Comments on Conservation of Energy and Momentum. (C) Genet, G. and Ebbesen, T., "Light in tiny holes", Nature (2007). Used under fair use, 2018. ....	13
Figure 6. Cosine Squared Dependence of Transmission Intensity on Incident Light Polarization. DiMaio, J. and Ballato, J., "Polarization-dependent transmission through subwavelength anisotropic aperture arrays", Optical Society of America (2006). Used under fair use, 2018. ....	14
Figure 7. Diagram of Surface Plasmon Polariton Excitation.....	21
Figure 8. Importance of Azimuthal Angle in Achieving Polarization Conversion .....	25
Figure 9. Multi-mode regime model.....	28
Figure 10. Standing waves from Brillouin zone boundaries.....	29
Figure 11. Analysis of Degenerate Bloch-SPP Modes from K-Space Diagrams.....	33
Figure 12. Experimental set-up and SEM image of nanohole array.....	38
Figure 13. Experimentally Observed Extraordinary Optical Transmission for $\phi = 0^\circ$ .....	40
Figure 14. Experimentally Observed Extraordinary Optical Transmission for $\phi=22^\circ$ .....	42
Figure 15. Typical user interface of Lumerical FDTD simulations.....	46

Figure 16. Simulated transmission for $\phi = 0^\circ$ . .....	47
Figure 17. Simulated transmission for $\phi = 0-22^\circ$ .....	49
Figure 18. Importance of Incident Polarization in Bloch-SPP Excitation and EOT. ....	52
Figure 19. Importance of Angle of Incidence in Bloch-SPP Excitation and EOT .....	54
Figure 20. Comparison of Bloch-SPPs on front and back surfaces of nanohole array.....	56
Figure 21. Multi-mode regime – hybridized Bloch-SPP mode case. ....	58

## List of Tables

Table 1. Role of Parameters.....	34
Table 2. Lumerical FDTD simulation parameters .....	45
Table 3. Analytically expected first order resonances for $\phi=0^\circ$ .....	48
Table 4. Simulated $\phi=0^\circ$ - Categorizing single-mode EOT and multi-mode EOT .....	48
Table 5. Analytically expected first order resonances for $\phi=22^\circ$ .....	49
Table 6. Simulated $\phi=22^\circ$ - Categorizing single-mode EOT and multi-mode EOT .....	49

# Chapter 1. Introduction

In 1998, Ebbesen, Lezec, Ghaemi, and Wolff published a paper<sup>1</sup> observing extraordinary optical transmission which would ignite a decades-long quest (and over 7500 citations) to understand the physics underlying their observation – the behavior of surface plasmon polaritons. Over the past 20 year, an improved understanding of surface plasmon polaritons has led to a variety of applications, including biomedical sensing<sup>12,32</sup>, energy harvesting<sup>13,31</sup>, and even information technology schemes<sup>14</sup>, unexpected to the original authors. However, much physics remains to be clarified regarding surface plasmon polaritons. As these gaps in understanding are filled, more applications of surface plasmon polaritons may arise.

The aim of this study is to use extraordinary optical transmission measurements and associated simulations to elucidate aspects of surface plasmon polaritons behavior, namely the role of incident light polarization on surface plasmon polaritons behavior and the hybridization of surface plasmon polaritons.

This chapter is intended to introduce the reader to extraordinary optical transmission (section 1.1), provide background regarding the current understanding of the behavior of surface plasmon polaritons and their role in extraordinary optical transmission (section 1.2), motivate our experiments by underlining the importance of polarization effects and polarization conversion in extraordinary optical transmission (section 1.3), and finally outline the scope of our project (section 1.4).

## 1.1. Extraordinary Optical Transmission (EOT)

In 1998, Ebbesen, Lezec, Ghaemi, Thio, and Wolff published observed that when light is shown on a thin metal film (~100nm thickness) perforated with an array of subwavelength holes (~100nm diameter) “the transmission efficiency can exceed unity (when normalized to the area of the holes), which is orders of magnitude greater than predicted by standard aperture theory”<sup>1</sup>. Specifically, the spectrum of the transmission through the nanohole array (figure 1) shows that at specific wavelengths “more than twice as much light is transmitted as impinges directly on the holes”. To put this in perspective, in classical electromagnetic aperture theory the transmission through nanoholes is expected to scale as  $\left(\frac{\text{radius of hole}}{\text{incident light wavelength}}\right)^4$ , leading to a predicted transmission efficiency on the order of  $10^{-3}$  (whereas the measured value was 2)<sup>11</sup>. The phenomena of transmission through nanohole arrays of intensity orders of magnitude greater than that expected from classical theories was termed “extraordinary optical transmission” (EOT).

To investigate the origin of this peculiar observation, Ebbesen et al investigated the dependence of the transmission spectra on various parameters such as lattice periodicity, film thickness, and angle of incidence<sup>1</sup>. They found that the wavelength of the transmission peaks was strongly correlated with lattice constant. In contrast, changing the film thickness had no effect on the wavelength of the peaks, but transmission did decrease as film thickness was increased. Most surprisingly, increasing the angle of incidence from 0° (normally incident light) to 2° caused some of the transmission peaks to split into two peaks at wavelengths slightly higher than and slightly lower than the wavelength of the original transmission peak. Based on these observations, Ebbesen et al suggested that the EOT phenomena was due to surface plasmon

polaritons (SPPs) – a quasiparticle originating from the coupling between the incident light photons and the electrons on the surface of the metal.

In the two decades following this seminal work, many ideas were presented for how SPPs mediate EOT. In 2001, Martin-Moreno et al. proposed that “EOT is due to tunneling through surface plasmons”<sup>3</sup>. In the same year, Krishnan et al suggested that “holes behave like subwavelength cavities for the evanescent waves coupling the SPs on either side of the film. The reflection at either end of the cavity is provided by the SP modes which act as frequency dependent mirrors.”<sup>4</sup> Perhaps the clearest model of how SPPs mediate EOT is explained by Altevischer et al in 2003: “in a simple picture, the incident light gets through because it first excites surface plasmons on the front side of the metal layer, which then couple through the holes to surface plasmons on the back side, which finally reradiate in the form of light”<sup>17</sup>. This picture, which decomposes the SPP mediated EOT process into a coupling-in process and a coupling-out process, is at the heart of the model presented in chapter 2 of this work.

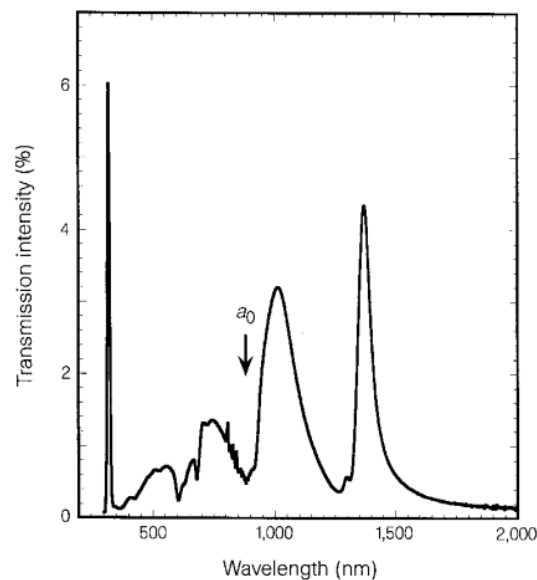


Figure 1. Transmission spectrum through nanohole array showing original observation of EOT. Ebbesen, T., et al., "Extraordinary optical transmission through sub-wavelength hole arrays", *Letters to Nature* (1998) 667-669. Used under fair use, 2018.

## 1.2. Surface Plasmon Polaritons (SPPs)

This section begins with a derivation of the fundamental physics which give rise to SPPs (section 1.2.1). This derivation is applied to nanohole arrays, and the aspects of the process of SPPs mediating EOT which are understood in literature are highlighted (section 1.2.2 and section 1.2.3). Finally, the aspects of SPPs mediating EOT for which there is no consensus (the role of incident light polarization) are presented (section 1.2.4).

### 1.2.1. Deriving the SPP Dispersion Relation

Surface plasmon polaritons (SPPs) are collective electron oscillations at a metal-dielectric interface driven by an incident electromagnetic field, as shown in figure 2. These coupled light-electron excitations propagate along and are confined to a metal-dielectric interfaces. Following the approach in Stefan Maier's 2007 "Plasmonics: Fundamentals and Applications" textbook, these properties can be derived by applying Maxwell's equations to the boundary between a metal, in which electrons are free to respond quickly to external electromagnetic fields therefore damping the propagation of electromagnetic fields, and a dielectric, in which free electrons are not readily present and electromagnetic fields can therefore propagate.

In the absence of external charge and current densities, Maxwell's curl equations and the constitutive equations can be combined to derive:

$$\nabla \times \nabla \times \vec{E} = -\mu_0 \left( \frac{\partial^2 \vec{D}}{\partial t^2} \right) \rightarrow \nabla \left( -\frac{1}{\epsilon} \vec{E} \cdot \nabla \epsilon \right) - \nabla^2 \vec{E} = -\mu_0 \epsilon_0 \epsilon \frac{\partial^2 \vec{E}}{\partial t^2} \quad (1.1)$$

where  $\vec{E}$  and  $\vec{D}$  are the usual electric fields related by the constitutive relations,  $\mu_0$  and  $\epsilon_0$  are physical constants, and  $\epsilon$  is the dielectric function (in general varying with wavelength  $\lambda$  and

position  $\vec{r}$ ) which characterizes a material's response to electromagnetic fields based on the behavior of its electrons.

When the dielectric function  $\epsilon$  is constant over distances on the order of the wavelength of the excitation field within a given material, and assuming harmonic time dependence of the fields, equation 1.1 simplifies to the well-known wave equation:

$$\nabla^2 \vec{E} - \frac{\epsilon}{c^2} \frac{\partial^2 \vec{E}}{\partial t^2} = 0 \rightarrow \nabla^2 \vec{E} + k_0^2 \epsilon \vec{E} = 0 \quad (1.2)$$

where  $k_0 = \frac{\omega}{c}$  is the wavevector of the propagating wave in vacuum. An analogous wave equation can be obtained for the magnetic field  $\vec{H}$ .

Defining the  $z$  axis as the direction along which the materials change and therefore the direction along which  $\epsilon$  varies, and defining the  $x$  axis as the axis on the metal-dielectric interface along which the wave propagates (see figure 2), we can obtain the following set of coupled equations:

$$\frac{\partial E_y}{\partial z} = -i\omega\mu_0 H_x \quad (1.3a)$$

$$\frac{\partial E_x}{\partial z} - i\beta E_z = i\omega\mu_0 H_y \quad (1.3b)$$

$$i\beta E_y = i\omega\mu_0 H_z \quad (1.3c)$$

$$\frac{\partial H_y}{\partial z} = i\omega\epsilon_0 \epsilon H_x \quad (1.3d)$$

$$\frac{\partial H_x}{\partial z} - i\beta H_z = -i\omega\epsilon_0 \epsilon E_y \quad (1.3e)$$

$$i\beta H_y = -i\omega\epsilon_0 \epsilon E_z \quad (1.3f)$$

This system only allows solutions when either only the  $E_x, E_z,$  and  $H_y$  components are nonzero (TM solutions) or when only the  $H_x, H_z,$  and  $E_y$  components are nonzero (TE solutions). For the TM solutions, equations (1.3a-f) lead to:

$$H_y(z) = A_2 e^{i\beta x} e^{-k_2 z} \quad (1.4a)$$

$$E_x(z) = iA_2 \frac{1}{\omega \epsilon_0 \epsilon_2} k_2 e^{i\beta x} e^{-k_2 z} \quad (1.4b)$$

$$E_z(z) = -A_1 \frac{\beta}{\omega \epsilon_0 \epsilon_2} e^{i\beta x} e^{-k_2 z} \quad (1.4c)$$

when  $z > 0$ , and

$$H_y(z) = A_1 e^{i\beta x} e^{-k_1 z} \quad (1.4d)$$

$$E_x(z) = iA_1 \frac{1}{\omega \epsilon_0 \epsilon_1} k_1 e^{i\beta x} e^{-k_1 z} \quad (1.4e)$$

$$E_z(z) = -A_1 \frac{\beta}{\omega \epsilon_0 \epsilon_1} e^{i\beta x} e^{-k_1 z} \quad (1.4f)$$

when  $z < 0$ . In these equations,  $A_1$  and  $A_2$  are yet to be determined constants,  $\epsilon_1$  and  $\epsilon_2$  are the dielectric functions for the metal and the dielectric respectively,  $k_1$  and  $k_2$  are the wavevectors in the metal and the dielectric respectively, and  $\beta$  is the propagation constant of the traveling waves given by the wavevector in the direction of propagation.

From continuity of  $H_y$  and  $\epsilon E_z$  at the boundary,  $A_1 = A_2$  and:

$$\frac{k_2}{k_1} = -\frac{\epsilon_2}{\epsilon_1} \quad (1.5)$$

Since  $H_y$  has to fulfill the wave equation for TM modes, we obtain:

$$k_1^2 = \beta^2 - k_0^2 \epsilon_1 \quad (1.6a)$$

$$k_2^2 = \beta^2 - k_0^2 \epsilon_2 \quad (1.6a)$$

Combining equations (1.5) and (1.6a-b), we arrive at the dispersion relation of SPPs propagating along a metal-dielectric interface:

$$\beta = k_{SPP} = k_0 \sqrt{\frac{\epsilon_1 \epsilon_2}{\epsilon_1 + \epsilon_2}} \quad (1.7)$$

The frequency dependence of the SPP wavevector, which in equation (1.7) is hidden in the dielectric functions, can be made explicit by assuming that the dielectric function of the dielectric is independent of frequency and the dielectric function of the metal follows the Drude free electron gas model:

$$\epsilon(\omega) = \epsilon_0 \left(1 - \frac{\omega_p^2}{\omega^2 + i\Gamma_p \omega}\right) \quad (1.8)$$

where  $\epsilon_0$  is the permittivity of free space,  $\Gamma_p$  is the phenomenological collision frequency of individual electrons which leads to absorption, and  $\omega_p$  is the plasma frequency at which electrons oscillate and depends only on the metal properties through the equation:

$$\omega_p = \sqrt{\frac{Ne^2}{\epsilon_0 m}} \quad (1.8b)$$

where  $N$  is the conduction electron density,  $e$  is the electron charge, and  $m$  is the electron mass.

In conclusion, we have derived the frequency dependence of the SPP wavevector (equation 1.7), which relates an SPP's momentum to its energy. This relation forms the basis for much of the physics discussed in this work.

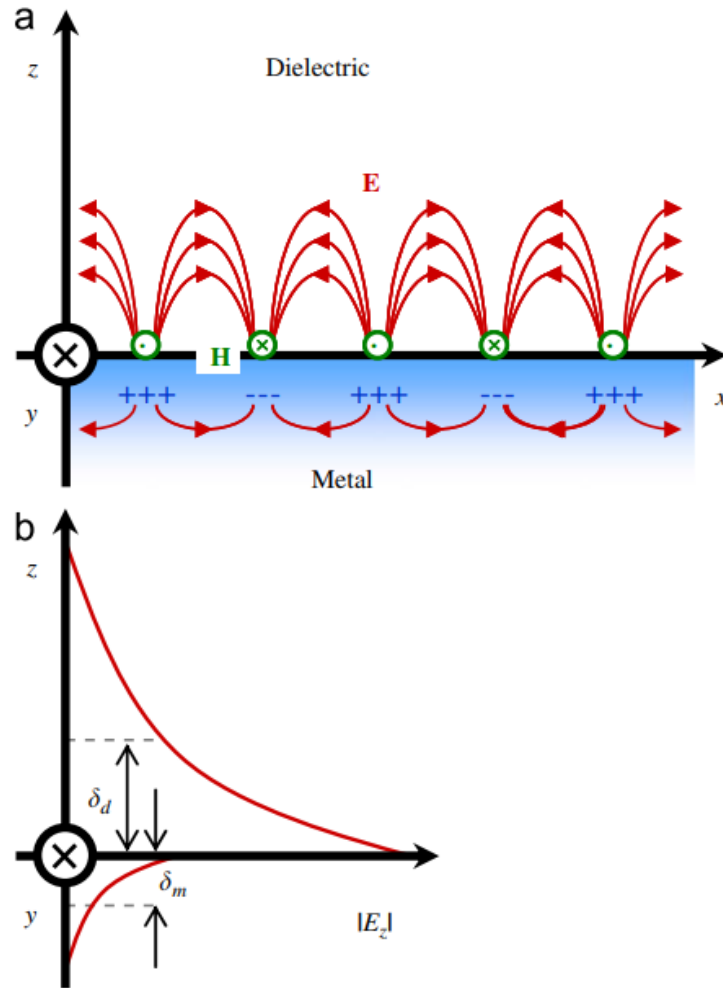


Figure 2. Schematic of SPP excitation. Lee, B. et al., "The use of plasmonics in light beaming and focusing", *Progress in Quantum Electronics* (2010) 47-87. Used under fair use, 2018.

### 1.2.2. Role of Energy and Momentum in SPP Excitation on Nanohole Arrays

Since free space light has a smaller wavevector than SPPs, free space light can only couple into SPPs if the momentum mismatch is overcome. In periodic structures with a given lattice, the Grating momentum from the reciprocal space of the lattice can be used to overcome the momentum mismatch (figure 3). As figure 3 shows, as only the in-plane component of the incident light wavevector can contribute to SPP excitation, the momentum provided by the incident light can be even less than the lightline dispersion relation, further highlighting the

importance of the Grating momentum in overcoming the momentum mismatch. In this case, the SPPs are termed “Bloch-SPPs”, to specify the origin of the extra momentum.

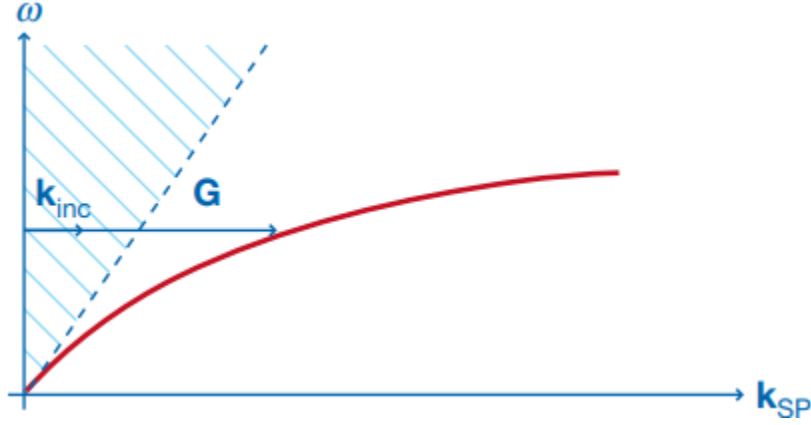


Figure 3. SPP dispersion relation. Genet, G. and Ebbesen, T., "Light in tiny holes", Nature (2007). Used under fair use, 2018.

The wavevector of the SPP is formed from the sum of the incident light wavevector (in the plane of the metal-dielectric interface to which the SPP is constrained) and the Grating momentum wavevector:<sup>11</sup>

$$\vec{k}_{SPP_{m,n}} = \vec{G}_{m,n} + \vec{k}_{||} \quad (1.9)$$

where  $\vec{G}_{m,n}$ , is the Grating vector with the indices of (m,n),  $\vec{k}_{||}$  is the in-plane wavevector of the incident light, and  $\vec{k}_{SPP_{m,n}}$  is the wavevector of the Bloch-SPP mode with the indices of (m,n)

From the geometry shown in figure 4,

$$\vec{G}_{m,n} = m \frac{2\pi}{P} \hat{x} + n \frac{2\pi}{P} \hat{y}, \quad (1.10)$$

$$\vec{k}_{||} = \frac{2\pi}{\lambda} \sin(\theta) \cos(\phi) \hat{x} + \frac{2\pi}{\lambda} \sin(\theta) \sin(\phi) \hat{y} \quad (1.11)$$

where P is the periodicity of the square lattice in nanohole arrays,  $\theta$  is the angle of incidence, and  $\phi$  is the azimuthal angle.

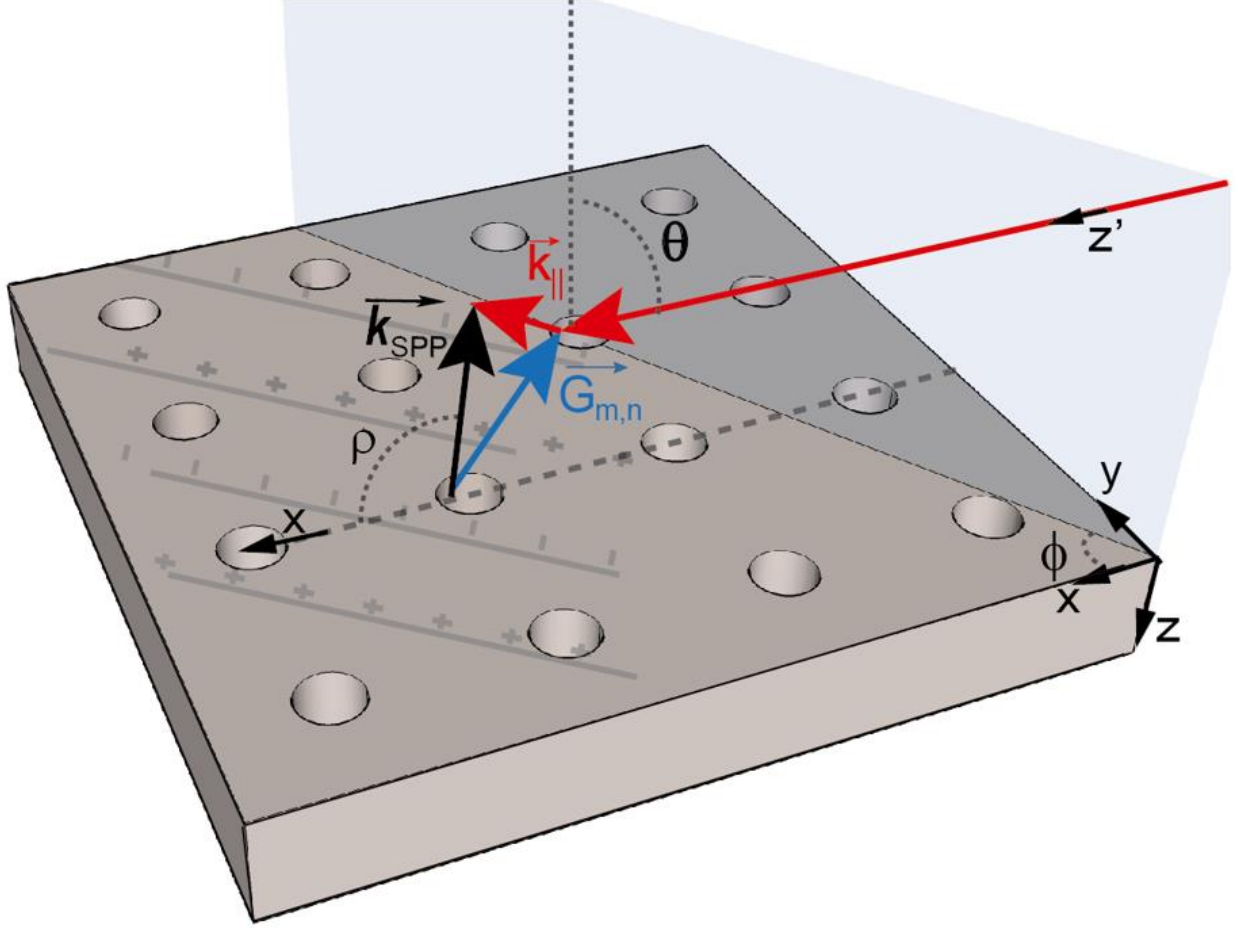


Figure 4. Geometry involved in SPP excitation

Schematic illustration of the nanohole array on which incident light with in plane wavevector  $k_{||}$  couples to the Grating momentum  $G_{ij}$  supported by the structure resulting in the (i,j) Bloch-SPP mode being excited and propagating in the direction in the direction of  $k_{SPP}$ . Relevant geometrical parameters referenced in the analytical model are defined.

For incident light to be at the resonant wavelength  $\lambda = \lambda_{SPP_{m,n}}$  allowing the (m,n) Bloch-SPP mode to be excited, the incident light wavelength must satisfy:

$$\left(\frac{2\pi}{\lambda_{SPP_{m,n}}}\right)^2 \frac{\epsilon_{metal}\epsilon_{dielectric}}{\epsilon_{metal}+\epsilon_{dielectric}} = (2\pi)^2 \left[ \left(\frac{m}{P} + \frac{\sin(\theta)\cos(\phi)}{\lambda_{SPP_{m,n}}}\right)^2 + \left(\frac{n}{P} + \frac{\sin(\theta)\sin(\phi)}{\lambda_{SPP_{m,n}}}\right)^2 \right] \quad (1.12)$$

where the left-side equals  $|\vec{k}_{SPP_{m,n}}|^2$  from the dispersion relation of SPPs at metal-dielectric interface (derived in section 1.2.1) and the right-side equals  $|\vec{k}_{SPP_{m,n}}|^2$  from equation (1.9).

When the wavelength of incident light satisfies equation (1.12) for multiple (m,n) pairs for fixed angle of incidence and azimuthal angle ( $\theta, \phi$ ), multiple Bloch-SPP modes can be simultaneously excited. While this work primarily develops a model for EOT due to single mode Bloch-SPP excitation, extending this model to the multi-mode regime is discussed in section 2.4 and further investigated in section 4.6.

### 1.2.3. Comments on Dispersion Plots

The aim of this section is to distinguish between two types of dispersion plots used in this work and describe how both are useful in understanding k-space diagrams used throughout this work. Ideally, this section will help avoid confusion later in the work.

All SPPs must satisfy the general SPP dispersion relation derived in section derived in section 1.2.1 (reproduced as figure 5A), which relates the magnitude of the wavevector representing the SPP ( $|\vec{k}_{SPP}|$ ) to its resonant energy, which is the energy of the incident light that can excite the SPP. In the previous section, we saw that Bloch-SPPs of various modes can be excited depending on how the structure bridges the momentum mismatch between free space light and SPPs (through different (m,n) modes of  $\vec{G}_{m,n}$ ). The general SPP dispersion relation makes no reference to various SPP modes, as it just outlines a condition that all SPP modes must satisfy. To understand and compare the behavior of different Bloch-SPP modes, we must therefore consider a new type of dispersion plot.

The energy conservation equation (equation 1.12) derived in the previous section suggests that at fixed geometrical parameters (azimuthal angle  $\phi$  and angle of incidence  $\theta$ ) different (m,n) Bloch-SPP modes should have different resonant energies (given by  $\lambda_{SPP_{m,n}}$ ) at which incident light excites the Bloch-SPP mode. As the angle of incidence is swept from (for

example)  $\theta = 0^\circ$  to  $\theta = 40^\circ$ , each Bloch-SPP mode would have a different curve relating the resonant incident light energy as a function of angle of incidence (which can be represented as the magnitude of the in-plane incident light wavevector  $|\vec{k}_{||}|$ , as for fixed incident light energy there is a one to one relation between angle of incidence and magnitude of incident light wavevector). Figure 5B shows the dispersion relation for various Bloch-SPP modes when the azimuthal angle is set to  $\phi = 22^\circ$  and angle of incidence is swept (therefore sweeping  $|\vec{k}_{||}|$ ).

K-space diagrams are often utilized throughout this work as a Bloch-SPP mode's wavevector (shown in k-space diagrams) represents the propagation direction of the Bloch-SPP mode in real space. Conveniently, k-space diagrams such as the one shown in figure 5C also provide a concise platform to understand both types of dispersion plots described above. Figure 5C shows how the in-plane component of the incident light wavevector ( $\vec{k}_{||}$ , represented by red arrows) can couple to various Bloch-SPP modes of the Grating vector ( $\vec{G}_{m,n}$ , represented by blue arrows) to form the (m,n) Bloch-SPP mode wavevector ( $\vec{k}_{SPP_{m,n}}$ , represented by the black arrows) in accordance with the momentum equation (equation 1.9). Using the general SPP dispersion diagram, the magnitude of the wavevector representing the (m,n) Bloch-SPP mode ( $|\vec{k}_{SPP_{m,n}}|$ ) directly determines the resonant energy of that Bloch-SPP mode. Figure 5C specifically shows that due to the relative directions of the in-plane incident light wavevector ( $\vec{k}_{||}$ ) determined by the azimuthal angle ( $\phi = 22^\circ$ ) and the Grating vectors determined by the choice of (m,n), each Bloch-SPP mode has a different wavevector magnitude of  $\vec{k}_{SPP_{m,n}}$  and therefore a different resonant energy. Specifically, we see that at an angle of incidence  $\theta = 5^\circ$ , the resonant energies of the  $\{(-1,0), (0,-1), (0,1), (1,0)\}$  Bloch-SPP modes are  $\{1.80\text{eV}, 1.85\text{eV}, 1.90\text{eV}, 1.95\text{eV}\}$ . Meanwhile, at an angle of incidence  $\theta = 40^\circ$ , the resonant energies of the  $\{(-$

$(1,0)$ ,  $(0,-1)$ ,  $(0,1)$ ,  $(1,0)$  Bloch-SPP modes are  $\{1.45\text{eV}, 1.80\text{eV}, 2.20\text{eV}, 2.4\text{eV}\}$ . The k-space diagrams elucidate why the dispersion plots of certain Bloch-SPP modes can have negative slopes, which is unusual in regular dispersion diagrams. The understanding of the relationship between the two types of dispersion plots and how they relate to k-space diagrams developed in this section will be especially important in analyzing the data presented in chapters 3 and 4.

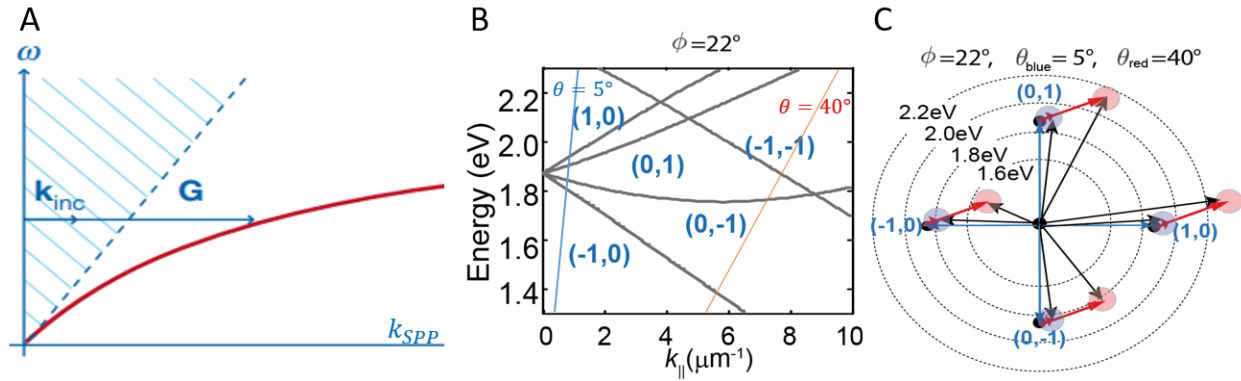


Figure 5. Comments on Conservation of Energy and Momentum. (C) Genet, G. and Ebbesen, T., "Light in tiny holes", *Nature* (2007). Used under fair use, 2018.

(A) Energy versus magnitude of SPP momentum (black arrows in figure A) dispersion curves. Reproduced from figure 3. (B) Energy versus incident light in-plane momentum (red arrow in figure C) dispersion curves for various Bloch-SPP modes. Reproduced from figure 14B. (C) Schematic showing k-space wavevectors associated with four Bloch-SPP modes. Reproduced from figure 11A.

#### 1.2.4. Role of Polarization in SPP Excitation on Nanohole Arrays

While section 1.2.2 shows that the role of incident light energy (or equivalently wavelength) and momentum is well understood, the understanding of the role of incident light polarization has remained limited.

As early as 2006, Dimaio et al considered the effect of rotating the incident light polarization on the intensity of the transmission<sup>20</sup>. While figure 6 shows a clear cosine squared dependence, this dependence of incident light polarization was simply ascribed to Malus' Law and no attempt was made to elucidate the microscopic origin. Furthermore, a simple,

deterministic way of predicting the optimal polarization angle does not appear to have been presented. More recently, in 2011 Zhao et al also noted the cosine squared dependence, but again no conceptual model was given to explain the microscopic physics<sup>22</sup>. Specifically, the direction of propagation of the excited SPP mode, which we believe to be crucial to determining the optimal incident light polarization angle (see section 2.2.1) is not discussed.

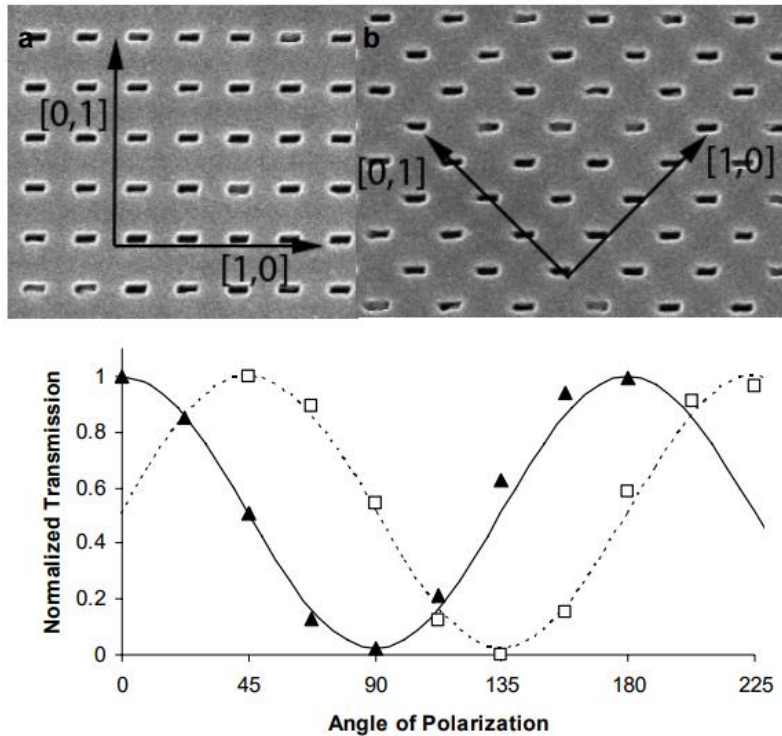


Figure 6. Cosine Squared Dependence of Transmission Intensity on Incident Light Polarization. DiMaio, J. and Ballato, J., "Polarization-dependent transmission through subwavelength anisotropic aperture arrays", *Optical Society of America* (2006). Used under fair use, 2018.

One of the first groups to tie the direction of the excited SPP mode to the dependence on incident light polarization was Altevischer et al in 2003, citing that "surface plasmon modes act as polarizers that pass only the polarization component that is aligned with their propagation directions."<sup>17</sup> Many groups supported this idea: in 2005 Genet et al wrote that "in our model the polarization of each surface wave is taken along its propagation direction"<sup>19</sup> and in 2010 Garcia-

Vidal et al explained that “if the normally incident light is polarized along the x direction, potential resonances owing to reciprocal lattice vectors pointing in the y direction [supporting SPP modes propagating close to the y direction] will not lead to strong transmission peaks”.<sup>13</sup>

While the above studies only comment on the role of incident light polarization in the coupling-in process of exciting the SPP modes, the role of polarization in the coupling-out has also been studied. In 2006, Isfort proposed that “upon retransformation of the surface plasmon polaritons wave into photons, these are emitted with a well-defined angle in the plane between the surface normal and the new electron propagation direction according to the SPP conditions...the polarization of the re-emitted light has to be parallel to the above mentioned plane”<sup>15</sup>, but did not directly tie the transmitted light polarization to the SPP propagation direction. In 2010, Garcia-Vidal went further to conclude that “together they [the polarization direction and phase of a given SPP mode] determine the polarization state of the transmitted light”<sup>13</sup>. While certainly impactful, all the observations and explanations mentioned above were all entirely phenomenological – no microscopic model presented appears to capture the underlying physics resulting in these explanations.

More recently, certain groups have explored the role of incident light polarization for non-circular holes. The most basic case is for elliptical hole arrays, in which Gordon et al in 2004<sup>33</sup>, Elliot et al in 2004<sup>25</sup>, Streltner et al in 2007<sup>21</sup>, and Lovera et al in 2012<sup>28</sup>. While transmission intensity is observed to depend on incident light polarization in these works, the dependence is not due to SPPs. For example, in the Streltner work, the cosine squared dependence is observed and an analytical model is developed to capture it, but in the limit as the elliptical holes become circular holes the dependence on incident light polarization vanishes, demonstrating that their model only captures the polarization dependence due to hole shape, not

SPPs. Polarization effects in more complicated hole shapes have been investigated, such as the Sierpinski carpet holes studied by Bao et al in 2007<sup>27</sup>, the S-shaped holes studied by Wu et al in 2013<sup>29</sup>, and the L-shaped holes studied in Zhu et al 2014<sup>34</sup> and Bouchon et al 2015<sup>35</sup>. In these studies, it seems that the polarization dependence is determined by the local hole shape rather than by the global SPP mode's propagation direction.

While the role of incident light polarization has been studied and experimentally a cosine squared relationship between transmission intensity and incident light polarization has been observed experimentally, much of the understanding of the physical origin remains limited. There is no consensus on the microscopic origin of this dependence. This may be due in large part to the fact that few, if any, groups have studied the role of incident light polarization in the near field (which is difficult to probe experimentally and must therefore be investigated numerically), where most of the interesting physics take place. This confusion manifests itself in recent claims such as those made by Wu et al in 2013<sup>29</sup> that “general nanohole structures only supporting the SPPs resonances cannot produce optical rotation. If the sample has a broken symmetry the optical rotation can be realized” and “polarization rotation angle for a single-layer metallic structure cannot exceed 45. A larger rotation than 45 would require multilayer structures” which are inconsistent with the models presented earlier in this section. Based on this, it is clear that a work is needed which presents a clear microscopic (using near field physics to explain far field measurable properties) picture of SPP mediated EOT including the role of incident light polarization.

### 1.3. Polarization Conversion

If the light reradiated by SPPs (usually as transmitted light, though in some studies as reflected light) has a different polarization than the incident light, then the phenomena of “polarization conversion” is said to have occurred. Polarization conversion is of interest for at least two reasons: (1) since polarization conversion is connected to the role of incident light polarization and is relatively easy to measure experimentally, it provides a convenient testbed for models of the role of incident light polarization in SPP mediated EOT, and (2) polarization conversion is crucial to many applications involving EOT which are discussed more thoroughly in chapter 5.

Much of the physics involved in polarization conversion remains to be understood. Cao et al appear to be a leading group in measuring polarization conversion involving nanohole arrays, although their work often relies on reflected light<sup>36-38</sup>. While their group successfully predicts polarization rotation angles between the incident and transmitted light, they do not seem to provide a clear microscopic model, highlighting the lack of such a model throughout the literature.

This work can also contribute in a more practical way by offering a fundamentally new way to achieve polarization conversion. In many studies (such as Lovera et al in 2012<sup>28</sup>), polarization conversion in EOT is achieved by using non-circular holes. In these cases, it seems that the polarization conversion occurs due to local effects within the holes rather than by the global behavior of SPP modes. While these works are relevant for applications requiring polarization conversion, they do not contribute much to the understanding of the polarization effects in SPP excitation. In addition, achieving polarization conversion due to a global property of the nanohole array (SPPs) instead of local properties of the nanohole array (hole shape) would

make the nanohole array's performance as a polarization converter more robust to fabrication imperfections (which affect the hole shape greatly but do not have strong impacts on the global properties).

#### 1.4. Scope of Project

This work is intended to fill a hole in the fundamental understanding of surface plasmon polaritons. While the role of incident light energy and momentum are well understood (section 1.2), much debate remains over the role of polarization (section 1.3). In this work, we present a microscopic model of the excitation of surface plasmon polaritons which captures the role of energy, momentum, and polarization.

One straightforward prediction of our model is polarization conversion. We use our model (presented in chapter 2) to design an experiment in which polarization conversion can be enabled by varying one parameter (azimuthal angle  $\phi$ ), experimentally measure the expected polarization conversion (chapter 3), and use numerical simulations to investigate the microscopic origin of the polarization conversion (chapter 4). In this way, polarization conversion is used to provide evidence supporting our model of the excitation of SPPs. As noted in section 1.3, while contributing to the physical understanding of polarization conversion, this work also contributes in a practical way by providing a novel approach to achieving polarization conversion based on global properties instead of local properties. As outlined in chapter 5 in the future works section, this novel approach to polarization conversion provides advantages over existing techniques that make it ideally suited for various applications.

## Chapter 2. Conceptual Model - Predicting EOT Polarization

### Conversion

In this chapter, we present a model describing the role of Bloch-SPPs in generating the EOT phenomena, including the often neglected role of incident light polarization, and comment on how our model predicts polarization conversion. We present a model capturing the process of energy coupling-in from free space to the plasmonic system (section 2.1) and coupling-out of the plasmonic system into free space as EOT (section 2.2) in the single mode regime. Analyzing the role of light polarization in these two processes, we predict the phenomenon of polarization conversion in EOT (section 2.3). We show how this model can be extended to describe the multi-mode regime (section 2.4). We then comment on the assumptions made in the model (section 2.5) and in which regimes these assumptions are valid (section 2.6). Finally, we summarize the role of each parameter in our model (section 2.7).

#### 2.1. Conceptual Model – Single Mode Regime Coupling-in Process

Under the dipole approximation, an isolated subwavelength nanohole impinged upon by light can be modeled as a dipolar scatter with dipole moment  $\vec{p}$  parallel to the direction of the current density, which in this case is given by the direction of in-plane electric field  $\vec{E}_{\parallel}$  of incident light (figure 7A). The nanohole dipole scatter can convert free-space light into 2D spherical Bloch-SPP waves at metal-dielectric interface. Figure 7B shows that a nanohole in a periodic nanohole array can also act as a dipolar scatter with dipole moment  $\vec{p}$  parallel to the direction of the current density. As the argument below indicates, the current density is parallel

to the Bloch-SPP propagation direction  $\vec{k}_{BSP}$  which has been well studied in literature (section 1.2).

When non-degenerate Bloch-SPPs are excited, a field  $\vec{E}_{BSP}$  is formed on the nanohole array with the in-plane component of  $\vec{E}_{BSP}$  leading to the charge distribution illustrated in figures 7B and 7C from which we can see that the in-plane component  $\vec{E}_{BSP,||}$  is parallel to  $\vec{k}_{BSP}$ . As the Bloch-SPP mode propagates along  $\vec{k}_{BSP}$ , the phase of  $\vec{E}_{BSP,||}$  evolves sinusoidally, driving an oscillating current  $\vec{J}_{SPP}$  parallel to  $\vec{k}_{SPP}$  (the out-of-plane component of  $\vec{E}_{BSP}$  does not contribute to  $\vec{J}_{BSP}$  as the electrons are constrained to the metal surface and therefore  $\vec{J}_{BSP}$  cannot have an out-of-plane component). As electrons are constrained to the metal and cannot travel through the holes, an oscillating build-up of charge forms on the edge of each hole as shown in figure 7B, effectively causing each hole to act as a localized surface plasmon. This leads to each hole acting as a dipole with dipole moment  $\vec{p}$  along the direction of the current density  $\vec{J}_{BSP}$ , and so  $\hat{p} = \hat{k}_{BSP}$ .

For incident light energy to optimally couple into the Bloch-SPP mode through the dipole scatter, the polarization of the incident light needs to be parallel to the dipole direction. Using Malus' Law, the coupling of incident light with an arbitrary polarization will be reduced from the coupling of light with the ideal polarization by a factor defined as the ‘‘coupling-in efficiency’’,

$$\text{Coupling – in efficiency} = \cos^2(\alpha_{||} - \rho_{m,n}). \quad (2.1)$$

In this equation,  $\alpha_{||}$  is the angle between the incident light polarization direction  $\hat{E}_{||}$  and the x axis (defined in figure 4) and  $\rho_{m,n}$  is the angle between the  $\vec{k}_{BSP,m,n}$  and the x axis. From equations (1.9)-(1.11), we find that

$$\rho_{m,n} = \tan^{-1} \left( \frac{\frac{\sin(\theta) \sin(\phi) + \frac{n}{\lambda}}{\sin(\theta) \cos(\phi) + \frac{m}{\lambda}}}{\frac{\sin(\theta) \sin(\phi) + \frac{n}{\lambda}}{\sin(\theta) \cos(\phi) + \frac{m}{\lambda}}} \right) \quad (2.2)$$

and

$$\alpha_{||} = \tan^{-1} \left( \frac{[\cos(\theta) \sin(\phi) \cos(\alpha) + \sin(\alpha) \cos(\phi)]}{[\cos(\theta) \cos(\phi) \cos(\alpha) - \sin(\alpha) \sin(\phi)]} \right). \quad (2.3)$$

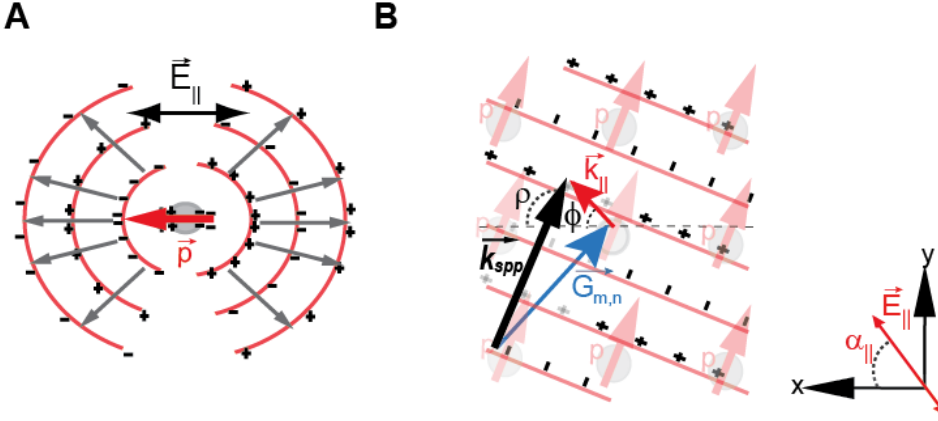


Figure 7. Diagram of Surface Plasmon Polariton Excitation.

(a) Schematic illustration of a single nanohole acting as a dipolar scatter polarized in direction  $p$  emitting spherical wave. (b) Schematic illustration of a nanohole array supporting a Bloch-SPP mode propagating in direction  $\hat{k}_{BSP}$ .

### 2.1.1. Derivation of Optimal Polarization Angle

We begin with the postulate that optimal coupling between the free space incident light and a given SPP mode is achieved when

$$\alpha_{||} = \alpha_{||,opt}(m,n) = \rho_{m,n} \quad (2.4)$$

where  $\alpha_{||}$  is the angle from the x axis (defined in figure 4) to the direction of the projection of the incident light electric field onto the metal film interface,  $\alpha_{||,opt}(m,n)$  is used to represent the optimal such angle for coupling free space incident light to the  $(m,n)$  Bloch-SPP mode, and  $\rho_{m,n}$

is the angle from the x axis to the propagation direction of the (m,n) Bloch-SPP measured counter-clockwise.

From the geometry presented in figure 4, the direction of the incident light electric field  $\hat{e}$  is given by:

$$\hat{e} = \hat{x}' \cos(\alpha) + \hat{y}' \sin(\alpha) \quad (2.5)$$

$$= \cos(\alpha) [\hat{x} \cos(\theta) \cos(\phi) + \hat{y} \cos(\theta) \sin(\phi) + \hat{z} \sin(\theta)] + \sin(\alpha) [-\hat{x} \sin(\phi) + \hat{y} \cos(\phi)] \quad (2.6)$$

$$= \hat{x}[\cos(\alpha) \cos(\theta) \cos(\phi) - \sin(\alpha) \sin(\phi)] + \hat{y}[\cos(\alpha) \cos(\theta) \sin(\phi) + \sin(\alpha) \cos(\phi)] + \hat{z}[\cos(\alpha) \sin(\theta)] \quad (2.7)$$

Defining  $\hat{e}_{||}$  as the direction of the projection of the incident light electric field onto the plane parallel to the metal-dielectric interface, we get:

$$\hat{e}_{||} = \hat{x}[\cos(\alpha) \cos(\theta) \cos(\phi) - \sin(\alpha) \sin(\phi)] + \hat{y}[\cos(\alpha) \cos(\theta) \sin(\phi) + \sin(\alpha) \cos(\phi)] \quad (2.8)$$

Defining  $\alpha_{||}$  as the angle between  $\hat{x}$  and  $\hat{e}_{||}$ , we get:

$$\alpha_{||} = \tan^{-1} \left( \frac{\cos(\alpha) \cos(\theta) \sin(\phi) + \sin(\alpha) \cos(\phi)}{\cos(\alpha) \cos(\theta) \cos(\phi) - \sin(\alpha) \sin(\phi)} \right). \quad (2.9)$$

Since optimal coupling is achieved when

$$\alpha_{||} = \alpha_{||,opt(m,n)} = \rho_{m,n}, \quad (2.10)$$

we can equate the optimal polarization angle to the (m,n) Bloch-SPP mode propagation direction:

$$\frac{\cos(\alpha) \cos(\theta) \sin(\phi) + \sin(\alpha) \cos(\phi)}{\cos(\alpha) \cos(\theta) \cos(\phi) - \sin(\alpha) \sin(\phi)} = \tan(\rho_{m,n}). \quad (2.11)$$

Simplifying and solving for the incident polarization angle  $\alpha$ :

$$\frac{\cos(\theta) \sin(\phi) + \tan(\alpha) \cos(\phi)}{\cos(\theta) \cos(\phi) - \tan(\alpha) \sin(\phi)} = \tan(\rho_{m,n}) \quad (2.12)$$

$$\cos(\theta) \sin(\phi) + \tan(\alpha) \cos(\phi) = \cos(\theta) \cos(\phi) \tan(\rho_{m,n}) - \tan(\alpha) \sin(\phi) \tan(\rho_{m,n}) \quad (2.13)$$

$$\tan(\alpha) [\cos(\phi) + \sin(\phi) \tan(\rho_{m,n})] = \cos(\theta) \cos(\phi) \tan(\rho_{m,n}) - \cos(\theta) \sin(\phi) \quad (2.14)$$

$$\tan(\alpha) = \frac{\cos(\theta) \cos(\phi) \tan(\rho_{m,n}) - \cos(\theta) \sin(\phi)}{\cos(\phi) + \sin(\phi) \tan(\rho_{m,n})}. \quad (2.15)$$

Recall from section 2.1 that the propagation direction of the (m,n) Bloch-SPP mode is given by:

$$\rho_{m,n} = \tan^{-1} \left( \frac{\frac{\sin(\theta) \sin(\phi)}{\lambda} + \frac{n}{P}}{\frac{\sin(\theta) \cos(\phi)}{\lambda} + \frac{m}{P}} \right). \quad (2.2)$$

Therefore, equation 2.15 gives the incident light polarization angle that will optimally excite the (m,n) Bloch-SPP mode in terms of geometrical parameters: azimuthal angle  $\phi$ , incident light angle of incidence  $\theta$ , resonant wavelength  $\lambda$  (determined by (m,n) and  $\theta$  through dispersion relations), and lattice constant P.

## 2.2. Conceptual Model – Single Mode Regime Coupling-out Process

For plasmonic nanohole arrays in the homogenous refractive index environment, the excitation of a Bloch-SPP mode on the front surface of the nanohole array can result in the excitation of the same Bloch-SPP mode on the back surface of the nanohole array with a phase

difference by evanescent field coupling through nanohole arrays (see section 4.5). In analogy to the coupling-in process described above, the periodic array of nanoholes can provide additional grating momentum to bridge the momentum mismatch and diffract Bloch-SPPs on the back interface into transmitted light in free space. Therefore, the polarization state of the transmitted light in EOT depends on the direction of induced dipole moment ( $\vec{p}$ ) of nanoholes and thus on the propagation direction of Bloch-SPPs during the coupling-out process.

The polarization state of transmitted light can be characterized with an analyzer at various rotational angles  $\beta$  measured counter-clockwise from the  $x'$  axis (as figure 4 shows, the  $x'$  axis is itself rotated  $\phi$  counter-clockwise from the  $x$  axis). Based on our analytical model in single mode regime, the percentage the total transmitted light observed past the analyzer depends on analyzer angle  $\beta$  and follows Malus' Law as:

$$\text{Percent through } \beta \text{ analyzer} = \cos^2((\beta + \phi) - \rho_{m,n}) \quad (2.16)$$

where  $(\beta + \phi) - \rho_{m,n}$  is the angle between the excited Bloch-SPP mode and the analyzer direction.

### 2.3. Analysis of Single Mode Regime Polarization Conversion

Combining equations (2.1) and (2.16), the polarization conversion efficiency, given as the ratio of the intensity of the incident light with polarization along polarizer direction ( $\alpha$ ) to the intensity of the transmitted light with polarization direction along analyzer direction ( $\beta$ ), is proportional to:

$$\text{Polarization conversion efficiency} \propto \cos^2(\alpha_{\parallel} - \rho_{m,n}) \cos^2((\beta + \phi) - \rho_{m,n}). \quad (2.17)$$

Through equation (2.17), the model quantifies the degree of polarization conversion expected in EOT mediated by a Bloch-SPP in the single mode regime based on geometrical factors ( $\theta, \phi$  which enter through  $\alpha_{||}, \rho_{m,n}$ ). As equation (2.17) draws upon every aspect of our model, comparing the polarization conversion predicted from equation (2.17) to experimentally observed polarization conversion provides a pathway towards validating the entire model.

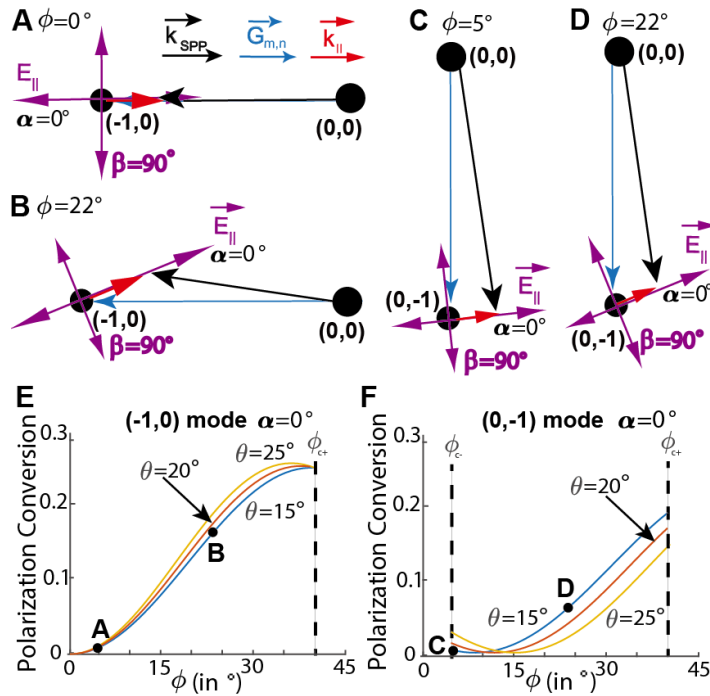


Figure 8. Importance of Azimuthal Angle in Achieving Polarization Conversion

(A-D) Schematic illustration of incident light with in-plane wavevector  $k_{||}$  coupling to the  $(-1,0)$  Grating vector mode resulting in the excitation of the  $(-1,0)$  Bloch-SPP mode when  $\phi = 0^\circ$  (A) and with  $\phi = 22^\circ$  (B). Analogously, coupling to the  $(0,-1)$  Grating vector mode is shown when  $\phi = 0^\circ$  (C) and with  $\phi = 22^\circ$  (D). (E-F) Plot of equation (4) for the  $(-1,0)$  Bloch-SPP mode (E) and the  $(0,-1)$  Bloch-SPP mode (F) for various  $\theta$  as  $\phi$  is swept, with necessary conditions on the azimuthal angle  $\phi$  to avoid degeneracies (see SI section 6).

As illustrated in figure 8, equation (2.17) predicts that polarization conversion in EOT depends strongly on the geometrical factor  $\phi$ . For polarization conversion to occur during EOT in the single mode regime, the Bloch-SPP wavevector  $\vec{k}_{BSP_{m,n}}$  and thus dipole moment  $\vec{p}$  of nanohole scatters must have a parallel component to both the in-plane electric field defined by  $\alpha_{||}$  and to

the analyzer orientation defined by  $\beta$ . While the angle of incidence  $\theta$  only rotates  $\vec{k}_{BSP_{m,n}}$  relative to  $\alpha$  and  $\beta$  slightly (at most 30 degrees, see figure 19B), the azimuthal angle  $\phi$  allows direct rotation of  $\alpha$  and  $\beta$  to any desired angle relative to  $\vec{k}_{BSP_{m,n}}$  (figure 8D). For the (-1,0) Bloch-SPP mode, figures 8A-B illustrate how rotating  $\phi$  from  $0^\circ$  to  $22^\circ$  rotates  $\vec{k}_{BSP_{m,n}}$  such that  $\vec{k}_{BSP_{m,n}}$  is no longer perpendicular to the  $\beta$  direction and the “coupling-out” process becomes enabled; similarly, for the (0,-1) Bloch-SPP mode figures 8C-D illustrate how rotating  $\beta$  from  $0^\circ$  to  $22^\circ$  enables the “coupling-in” process. Quantitatively, this is supported by figures 8E-F which show that for both the (0,-1) and (-1,0) Bloch-SPP modes equation (2.17) predicts that polarization conversion can be enabled by varying  $\phi$ .

## 2.4. Extending the Model to the Multi-Mode Regime

In certain cases, the energy conservation equation (1.12) is satisfied for multiple Bloch-SPP modes simultaneously (same angle of incidence, azimuthal angle, incident light wavelength). This is the case when the azimuthal angle is set to  $\phi = 22^\circ$ , the angle of incidence is set to  $\theta = 12^\circ$ , and the incident wavelength is set to  $\lambda = 575\text{nm}$ , as this configuration leads to the (1,0), (0,1) and (1,1) all simultaneously satisfying equation (1.12). The multi-mode regime can be understood by considering each pair of Bloch-SPP modes (if only two Bloch-SPP modes are excited considering one pair, if three Bloch-SPP modes are excited considering three pairs, and if  $n$  Bloch-SPP modes are excited considering  $\frac{n(n-1)}{2}$  pairs). When a pair of Bloch-SPP modes is simultaneously excited, interference between the Bloch-SPP modes leads to a standing wave in the direction perpendicular to the sum of their wavevectors, as illustrated in figures 9A-C for three different pairs of Bloch-SPP modes. Whereas in the single mode regime model there

are no standing waves and the charge distribution pattern is dominated by the propagation direction of the excited Bloch-SPP mode which in turn determine the dipole direction associated with each nanohole, in the multi-mode regime the standing wave dominates the charge distribution pattern on the nanohole array surface and therefore determines the direction of the dipole associated with each nanohole.

Figure 9 explicitly shows the standing waves that would form if the (0,1), (1,0), and (-1,-1) Bloch-SPP modes were to be simultaneously excited. The hybridization between these three Bloch-SPP modes can be understood by viewing each pair of Bloch-SPP modes as generating one standing wave through their interference (figures 6A-C), and therefore there being three dipole directions associated with each nanohole (figure 6D). Similarly to the single mode regime, the excitation of each dipole follows a cosine squared relationship between the dipole direction and the direction of the in-plane incident light electric field  $\vec{E}_{||}$ .

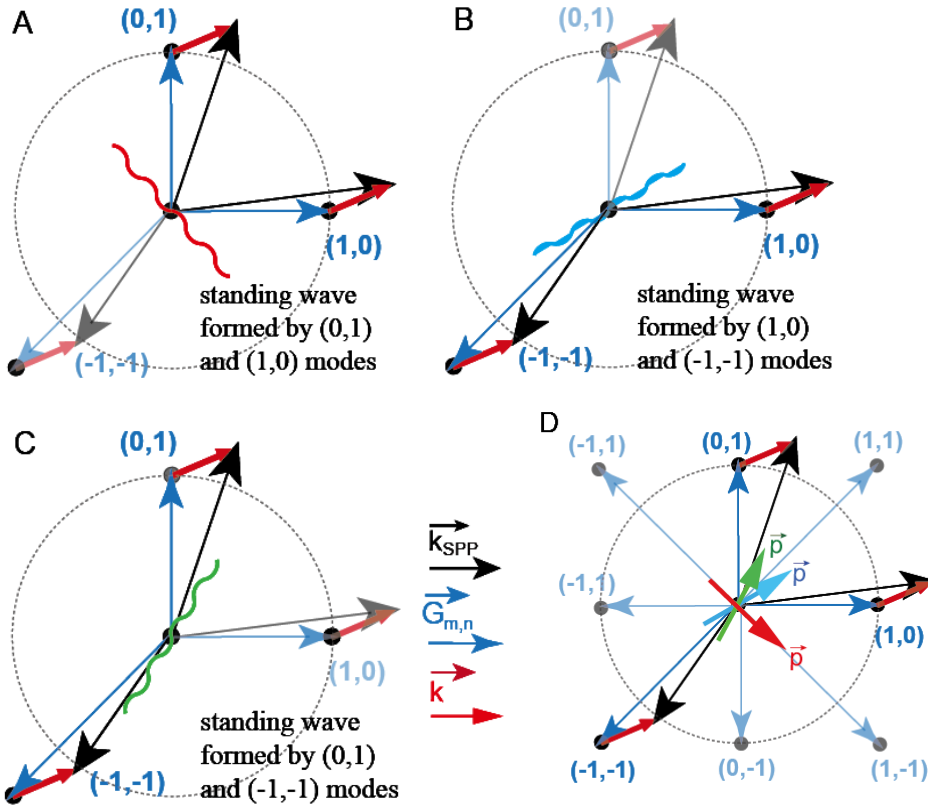


Figure 9. Multi-mode regime model.

(A) Schematic illustration of the standing wave formed by the interference of the  $(0,1)$  and  $(1,0)$  Bloch-SPP modes. (B) Standing wave formed by  $(1,0)$  and  $(-1,-1)$  Bloch-SPP modes. (C) Standing wave due to  $(0,1)$  and  $(-1,-1)$  Bloch-SPP modes. (D) Summary of the three standing wave directions that can be excited with an efficiency determined by the incident light polarization.

### 2.4.1. Standing Waves from Brillouin Zone Boundaries

This section aims to demonstrate how the standing wave model presented in section 2.4 is applicable in the case of Bloch-SPPs with wavevectors along the Brillouin zone. Figure 10A illustrates the well-known theorem in solid state physics that a given point in  $k$ -space is equivalent to the point translated by reciprocal lattice vectors in terms of crystal momentum (represented by blue arrows). Each red dot can be thought of as representing a given Bloch-SPP mode. While each of the Bloch-SPP modes represented by the red dots have equivalent crystal momentum, in this example each Bloch-SPP mode has a different energy (directly related to the magnitude of its wavevector).

Figure 10B specifies the general concept illustrated in figure 10A to the case of a momentum at a Brillouin zone boundary (represented by dashed lines). In this case, there is guaranteed to be two (or four) k-space locations which share not only the same crystal momentum but also the same energy. The two highlighted red dots in figure 10B represent the two k-space locations, representing Bloch-SPP modes, which share the same energy and therefore will be simultaneously excited. Figure 10C shows that when both Bloch-SPP modes are excited, the model developed in section 2.4 can be used to explain the existence of a standing wave. This means that each time a Bloch-SPP mode with a wavevector along a Brillouin zone boundary is excited, another Bloch-SPP mode will be simultaneously excited and therefore the standing wave model presented in section 2.4 is applicable.

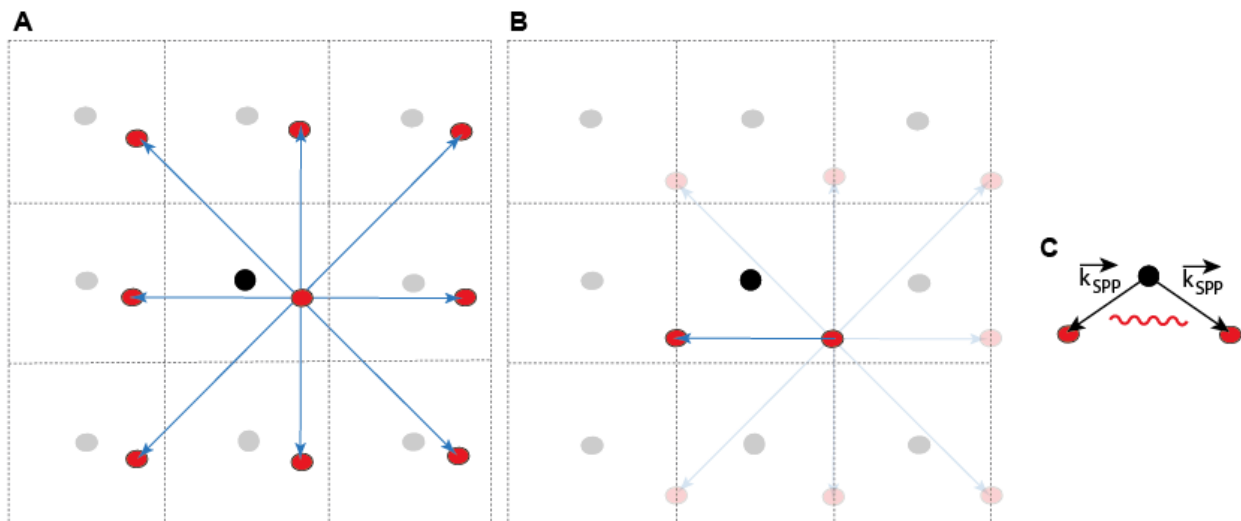


Figure 10. Standing waves from Brillouin zone boundaries.

(A) Illustration of various locations in k-space. The black dots represent reciprocal lattice points, the dashed lines represent the 1<sup>st</sup> Brillouin zone of each reciprocal lattice point, the center red dot represents a given k-space point, and the other red dots represent k-space points with equivalent crystal momentum connected by lattice vectors represented by blue arrows. (B) Specific case of illustration shown in figure S5A in which the k-space locations are along Brillouin zones. The two highlighted k-space locations share not only the same crystal momentum but also the same energy. (C) Schematic illustration of two excited Bloch-SPP modes and the direction of the standing wave formed from their interference.

## 2.5. Assumptions

In this section, the key assumptions of this model are presented. For each assumption, the necessity is highlighted and the justification is outlined.

The dipole approximation is used to represent the alternating electric field across each hole as a dipole, ignoring higher order terms in the multipole expansion. In the archetypical case of an atom scattering light, this approximation holds when the size of the atom is much less than the wavelength of the emitted light. In our model, the scatter are nanoholes instead of atoms. Therefore, since the size of the nanoholes ( $\sim 100\text{nm}$ ) is much smaller than the wavelength of Bloch-SPP waves or the emitted photons ( $\sim 700\text{nm}$ ), we are justified in approximating individual nanoholes as dipole scatters with their dipole moment  $\vec{p}$  aligned along the current density  $\vec{J}_{BSP}$ , and Bloch-SPP propagation direction  $\hat{k}_{BSP}$ .

The argument that  $\vec{J}_{BSP}$  follows  $\hat{k}_{BSP}$  implicitly assumed that only one Bloch-SPP mode was excited at a given wavelength. In the multi-mode regime where multiple Bloch-SPP modes are simultaneously excited, the current propagation direction is no longer well defined. Instead, the nature of the oscillating charge build-ups which allow each hole to be considered as a dipole is given by the direction of a standing wave. The physics of the multi-mode regime are discussed in section 4.6. Outside of this section, this entire work considers only the single-mode regime.

This model is entirely classical, and therefore we assume no quantum mechanical phenomena have significant effects. For example, if the nanohole diameter were on the order of the electrons' wavelengths, then quantum mechanical tunneling of the electrons through the holes would have to be considered. This would invalidate the picture of the holes presenting an

infinite potential barrier that the electrons cannot surmount, leading to the build-up of charge on the edge of the holes, culminating in our treatment of the nanoholes as dipoles.

## 2.6. Regimes of Validity

The assumptions used to develop our model (section 2.4) limit the regime in which our model is valid. Specifically, the dipole approximation and the quantum mechanical negligibility assumptions apply a constraint on the size of the nanoholes. For the dipole approximation to hold, the nanoholes can be no greater than a couple hundred nanometers in diameter. For quantum mechanical effects to be negligible, the nanoholes must be at least tens of nanometers in diameter. Our nanoholes are set to a fixed 100nm diameter throughout this experiment, thereby ensuring both of these assumptions are valid.

The more stringent assumption is that for the single mode regime model only one Bloch-SPP mode can be excited (multi-mode regime discussed in section 4.6). Another way to formulate this condition is that for fixed geometrical parameters (angle of incidence  $\theta$  and azimuthal angle  $\phi$ ) and at a given incident light wavelength, each Bloch-SPP mode must have a different energy. As the dispersion relation of Bloch-SPP shows that there is a one-to-one correspondence between Bloch-SPP energy and momentum (the curve in figure 3 is monotonically increasing), this is equivalent to each Bloch-SPP mode having a different momentum magnitude. K-space diagrams provide a useful tool to verify this condition: for the single mode regime to hold, the k-space vector of each Bloch-SPP mode must have a unique magnitude.

Figure 11 shows the k-space representation of each of the four first-order Bloch-SPP modes. Since the real space lattice is a 2D simple cubic (square) lattice, the reciprocal lattice is also a 2D simple cubic lattice, and therefore the Grating vectors which are elements of the reciprocal space are along the x and y axes. The magnitude of the Grating vectors is given by  $|\vec{G}| = \frac{2\pi}{P} = 15.7\mu m^{-1}$ . Meanwhile, the direction of the in-plane momentum of the incident light is at an angle  $\phi$  from the x axis measured counter-clockwise, and the magnitude is given by  $|\vec{k}_{||}| = \frac{2\pi}{\lambda_{SPP}} \sin(\theta) = 3.1\mu m^{-1}$  for typical values of the wavelength  $\lambda = 700\text{nm}$  and angle of incidence  $\theta = 20^\circ$ . Note that even for a fixed angle of incidence, each Bloch-SPP mode will have a slightly different  $|\vec{k}_{||}|$  as their resonant wavelengths are different. Note that the energy of the Bloch-SPP mode as calculated by plugging in the magnitude of  $|\vec{k}_{SPP_{m,n}}|$  into the dispersion relation (figure 3) must be equal to the energy associated with the incident light,  $E_{inc} = 2\pi\hbar c/\lambda_{SPP}$ , which is essentially the energy condition. As each Bloch-SPP mode has a linewidth, the position of the vector in reciprocal space representing in each Bloch-SPP mode is shown as a shaded circle.

Figure 11A establishes the single mode regime condition on the angle of incidence  $\theta$ . The blue shaded circles show that for small angle of incidence  $\theta < 5^\circ$ , all four Bloch-SPP modes are degenerate. This trend holds for any azimuthal angle  $\phi$ . In contrast, the red shaded circles show that at larger angle of incidence  $\theta$  this degeneracy is lifted due to the momentum from the incident light. Figure 11B establishes the single mode regime condition on the azimuthal angle  $\phi$ . Even at angle of incidences  $\theta$  satisfying the first condition (figure 11A), the blue shaded circles show that  $\phi = 0^\circ$  leads to a degeneracy between the (0,1) and the (0,-1) Bloch-SPP mode. Likewise,  $\phi = 45^\circ$  would lead to a degeneracy between the (1,0) and (0,1) pair and the (-1,0)

and (0,-1) pair which cannot be lifted by angle of incidence  $\theta$ . However, setting the azimuthal angle to an intermediate value such as  $\phi = 22^\circ$  allows the degeneracies to be lifted, as shown by the red shaded circles.

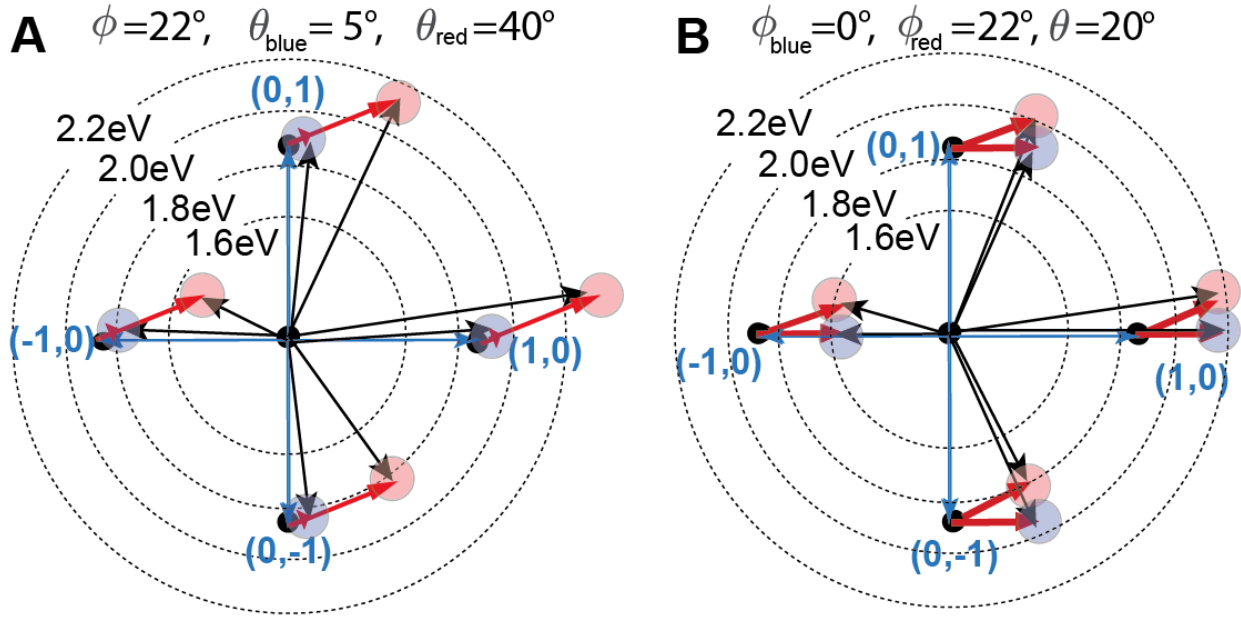


Figure 11. Analysis of Degenerate Bloch-SPP Modes from K-Space Diagrams

(A) Schematic showing that while the four first-order Bloch-SPP modes are degenerate for low angle of incidences (blue circles), the degeneracy can be broken by increasing the angle of incidence (red circles). (B) Schematic showing that while the (0,+1) Bloch-SPP modes are degenerate when the azimuthal angle is set to  $\phi = 0^\circ$  (blue circles) even at high angles of incidence, rotating the azimuthal angle to  $\phi = 22^\circ$  (red circles) lifts the degeneracy.

## 2.7. Role of Each Variable

Figure 4 illustrates several variables which all effect polarization conversion in EOT. Incident light properties such as wavelength  $\lambda$  and polarization angle  $\alpha$  are perhaps the most obvious parameters. Geometrical parameters such as the angle of incidence  $\theta$  and the azimuthal angle  $\phi$  are the most prevalent in this study. While fixed in this study, other geometrical

parameters such as lattice periodicity  $P$  and film thickness  $T$  are also of importance. Table 1 summarizes the importance of each of these parameters.

Table 1. Role of Parameters

Parameter	Value range	Importance
Incident light wavelength $\lambda$	From 530nm to 950nm experimentally; from 400nm to 1000nm in simulation	The incident light wavelength, for a fixed angle of incidence, determines which Bloch-SPP modes are excited. The incident light wavelength also contributes to the magnitude of the in-plane wavevector.
Incident light polarization angle $\alpha$	From 0 degrees to 180 degrees	The incident light polarization determines the degree to which the free space incident light can couple to the excited (m,n) Bloch-SPP mode. This variable has no impact in generating the reciprocal space diagrams and specifically no relevance in determining which Bloch-SPP mode is excited.
Angle of incidence $\theta$	From 0 degrees to 40 degrees	The angle of incidence, along with the incident light wavelength, determines which Bloch-SPP modes are excited, and can be used to lift the degeneracies between certain modes.
Azimuthal angle $\phi$	0 degrees and 22 degrees	The azimuthal controls the dispersion relations of each Bloch-SPP mode, and can be used to create degeneracies in the dispersion relations (meaning degeneracies that hold for all angle of incidences) when

		set to symmetric values such as $\phi = \{0^\circ, 45^\circ, 90^\circ\}$ . By rotating the azimuthal angle to $\phi = 22^\circ$ , the degeneracies can be lifted by the angle of incidence, allowing each Bloch-SPP mode to be addressed individually.
Periodicity P	Fixed at 400nm	The lattice periodicity is inversely proportional to the periodicity of the reciprocal space and therefore to the magnitude of the Grating vectors. See equation 1.10.
Film thickness T	Fixed at 100nm in experiment; from 60nm to 200nm in simulation	Determines coupling between Bloch-SPPs on front interface of nanohole array and back surface of the nanohole array. See section 4.5.

## Chapter 3. Experimental Results – Observing EOT Polarization

### Conversion

The chapter analyzes the data collected from two experiments. We first motivate these experiments as testbeds for the model developed in chapter 2 (section 3.1) and describe the experimental set-up (section 3.2). We then present the data from both experiments (sections 3.3 and 3.4) and draw conclusions (3.5).

#### 3.1. Motivation for Experiments

The motivation for measuring polarization conversion is two-fold: (1) polarization conversion allows us to test both the coupling-in and the coupling-out processes described in our conceptual model, thereby providing a pathway towards verifying our entire model; (2) the way in which we achieve polarization conversion in transmitted light is fundamentally new from the way polarization conversion has been achieved in the past, allowing a much more robust platform that can improve applications such as those noted in chapter 5. As explained in section 3.1.1, the azimuthal angle  $\phi$  is the angle that most directly enables or disables polarization conversion, and therefore is the main independent variable in the experiments.

##### 3.1.1. Importance of Azimuthal Angle $\phi$ in Achieving Polarization Conversion

The azimuthal angle  $\phi$  has a unique importance in the fundamental physics involved in SPP excitation as it is the only variable responsible for the presence or lack of degenerate dispersion relations (sections 2.5 and 2.6). This alone suggests that the azimuthal angle plays a key role in the experiments, as our model describes the single mode regime, and therefore the

dispersion relations must somehow be split so that each Bloch-SPP mode can be addressed individually. As figure 11 shows, the importance of the azimuthal angle from the perspective of fundamental physics translates to the azimuthal angle being key to the practical matter of generating polarization conversion (section 2.3).

### 3.2. Experimental Set-Up

All fabrication and experimental measurements were conducted by Dr. Wei Zhou under the supervision of Dr. Teri Odom at Northwestern University. The nanohole fabrication is similar to that described in a reference<sup>39</sup> and will not be explicitly covered in this work. This section describes the basic methods involved in the optical characterization.

Referring to the geometry presented in figure 12A, the nanohole sample in SiO<sub>2</sub> was set to an azimuthal angle  $\phi = 0^\circ$  and an incidence angle  $\theta = 0^\circ$ . The analyzer and polarizer were both set to  $\alpha = \beta = 0^\circ$ . White light was shown on the nanohole array at an incidence angle  $\theta = 0^\circ$ . The spectrum of the transmitted light was measured. The angle of incidence (in free space) was incremented by  $.1^\circ$  until  $\theta = 40^\circ$ , each time measuring the transmission spectrum. This process was repeated for a total of four combinations of polarizer and analyzer set-ups: ( $\alpha = 0^\circ, \beta = 0^\circ$ ), ( $\alpha = 0^\circ, \beta = 90^\circ$ ), ( $\alpha = 90^\circ, \beta = 0^\circ$ ), ( $\alpha = 90^\circ, \beta = 90^\circ$ ). Finally, the azimuthal angle was rotated to  $\phi = 22^\circ$  and the above process was repeated.

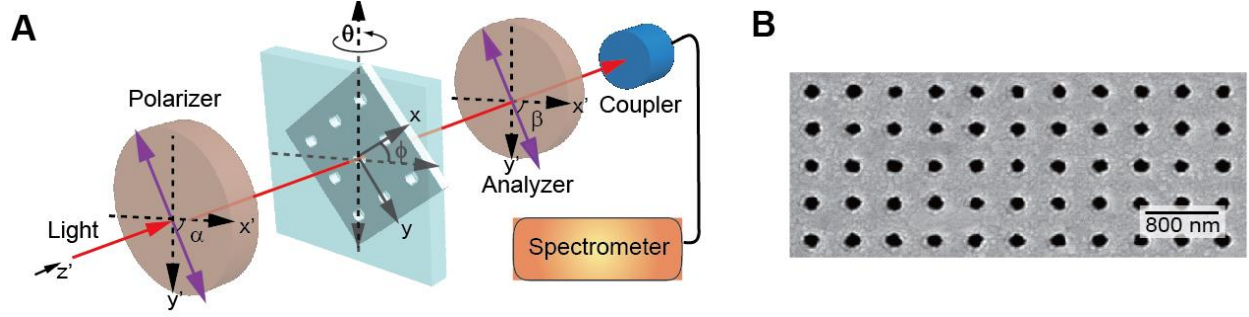


Figure 12. Experimental set-up and SEM image of nanohole array.

(A) Schematic illustration of the experimental set-up. Light polarized in a direction  $\alpha$  is incident on the nanohole array. Transmitted light is passed through a polarizer in the  $\beta$  direction before being measured.  $\hat{y}'$  sets the axis about which the nanohole is rotated and  $\hat{x}'$  and  $\hat{z}'$  define the plane of incidence (B) SEM image of the nanohole array used in the experiment.

### 3.3. $\phi = 0^\circ$ Experiment

In the first experiment,  $\phi$  is set to  $0^\circ$  leading to the first order Bloch-SPP modes having propagation directions as shown in figure 13A and dispersion relations shown in figure 13B. Figures 13C-13F show the observed transmission intensity for various incident light polarizations  $\alpha$  and analyzer direction  $\beta$ . Transmission observed in figure 13D and 13E represent polarization conversion, as the incident light polarizations  $\alpha$  and analyzer direction  $\beta$  are set to be orthogonal to one another. The transmission observed in figures 13C-F can be categorized into two classes. At energies below 1.8eV, the transmission is along the dispersion curves shown in figure 13B, indicating it is due to only one Bloch-SPP mode. In contrast, the transmission above 1.8eV is observed in between dispersion curves of various Bloch-SPP modes, suggesting that multiple Bloch-SPP modes are involved.

As can be seen from figure 13B, only the  $(-1,0)$  Bloch-SPP mode is nondegenerate and therefore is the subject of our focus. As seen in figure 13A,  $\phi = 0^\circ$  generates a symmetry between the structure supporting the Bloch-SPPs ( $\vec{G}_{-1,0}$ ) and the in-plane component of the

incident light wavevector ( $\vec{k}_{||}$ ) which leads to  $\vec{k}_{BSP_{-1,0}}$  and  $\vec{k}_{||}$  being parallel. From equation (2.1), this implies that the (-1,0) Bloch-SPP mode should be maximally excited when  $\alpha = 0^\circ$  ( $\vec{E}_{||}$  is parallel to  $\vec{k}_{||}$  so  $\alpha_{||} - \rho = 0^\circ$ ) and not excited when  $\alpha = 90^\circ$  ( $\alpha_{||} - \rho = 90^\circ$ ). Furthermore, since the transmitted light is polarized in the direction of  $\vec{k}_{BSP_{-1,0}}$ , the transmitted light should be polarized along the  $\hat{x} = \hat{x}'$  (since  $\phi = 0^\circ$ ) direction. This means it should maximally pass the polarizer when  $\beta = 0^\circ$  and be completely blocked by the polarizer when  $\beta = 90^\circ$ . Figure 13C-F, which show the transmission for various  $\alpha, \beta$ , confirm this as transmission along the (-1,0) Bloch-SPP mode is only observed when  $\alpha = 0^\circ$  and  $\beta = 0^\circ$  (figure 13C).

Several other features of the transmission are of interest. The transmission in figure 13F can be fully understood through our multi-mode regime model, as described in section 2.4 and numerically investigated in section 4.6. In this case, the (0,+1) Bloch-SPP modes interfere to form a standing wave in the y direction, which dominates the dipole direction of each hole. Therefore, this Bloch-SPP mode acts as if it were in the single mode regime with a Bloch-SPP wavevector in the y direction. This is consistent with transmission observed only when the incident light polarization is set to  $\alpha = 90^\circ$  (y direction) and the analyzer is set to  $\beta = 90^\circ$ . Figure 13C shows interesting multi-mode regime transmission involving the (0,+1), (-1,+1), and (1,0) Bloch-SPP modes. Analogously to the (0,+1) multi-mode regime, transmission due to these five Bloch-SPP modes can be understood from the discussion in sections 2.4 and 4.6.

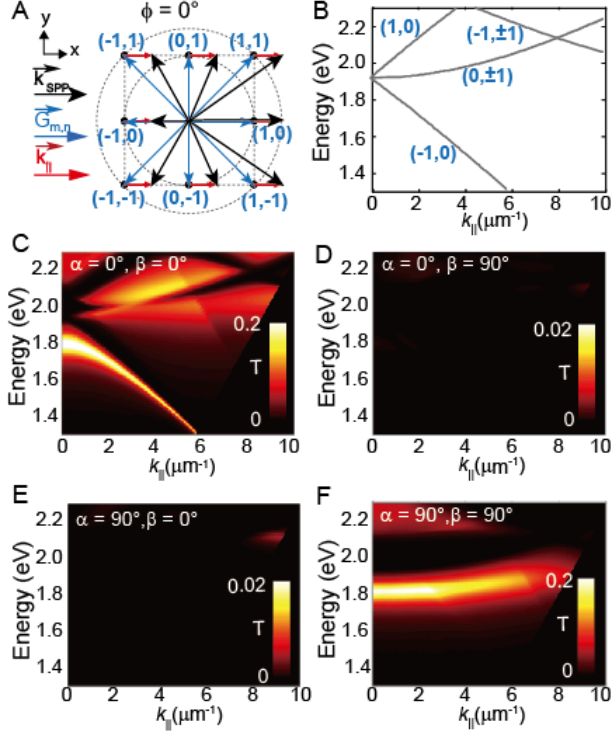


Figure 13. Experimentally Observed Extraordinary Optical Transmission for  $\phi = 0^\circ$

(A) Schematic illustration of incident light with in-plane wavevector  $\vec{k}_{\parallel}$  coupling to  $(m, n)$  first order Grating vector modes resulting in the excitation of the  $(m, n)$  Bloch-SPP mode when  $\phi = 0^\circ$ . (B) Plot of the dispersion relations of each Bloch-SPP mode. This figure shows what incident light wavelength (energy) satisfies the momentum equation with the  $(m, n)$  Bloch-SPP mode when the incident light is incident at an angle  $\theta$  ( $k_{\parallel} = \frac{2\pi}{\lambda} \sin(\theta)$ ). (C-F) Experimentally observed transmission with the azimuthal angle set to  $\phi = 0^\circ$ , the angle of incidence  $\theta$  is swept from 0 to 40 degrees, and the analyzer and polarizer directions  $(\alpha, \beta)$  are set to  $(0^\circ, 0^\circ)$  (figure 13C),  $(0^\circ, 90^\circ)$  (figure 13D),  $(90^\circ, 0^\circ)$  (figure 13E),  $(90^\circ, 90^\circ)$  (figure 13F).

### 3.4. $\phi = 22^\circ$ Experiment

In the second experiment  $\phi = 22^\circ$  which breaks the symmetry between the structure and the incident light wavevector. According to equation (13) this enables  $\alpha = 0^\circ \rightarrow \beta = 90^\circ$  and  $\alpha = 90^\circ \rightarrow \beta = 0^\circ$  polarization conversion as  $(\alpha_{\parallel} - \rho_{-1,0})$  is no longer constrained to  $0^\circ$  (in the case of  $\alpha = 0^\circ \rightarrow \beta = 90^\circ$ ) or  $90^\circ$  ( $\alpha = 90^\circ \rightarrow \beta = 0^\circ$ ), but rather can take on intermediate values, allowing both the coupling-in and coupling-out terms to be nonzero simultaneously

thereby enabling polarization conversion. Changing the azimuthal angle to  $\phi = 22^\circ$  also lifts the degeneracy between (0,1) and (0,-1) Bloch-SPP modes (see split dispersion relations in figure 14B) as  $\vec{k}_{\parallel}$  has a non-zero y-component, allowing our model to describe the (0,-1) Bloch-SPP mode. Equation (2.2) predicts that  $\rho_{-1,0} = 174.9^\circ$ ,  $\rho_{0,-1} = 103.9^\circ$ , meaning that both of these Bloch-SPP modes can be excited by both  $\alpha = 0^\circ$  ( $\alpha_{\parallel} = \phi = 22^\circ$ ) and  $\alpha = 90^\circ$  ( $\alpha_{\parallel} = \phi - 90^\circ \rightarrow 112^\circ$ ) incident light. Further, since the transmitted light is polarized in the  $\vec{k}_{SPP_{m,n}}$  direction, light transmitted by both Bloch-SPP modes would be detectable regardless of whether the polarizer is set up in the  $\beta = 0^\circ$  or  $\beta = 90^\circ$  configuration. Specifically, this means that the (0,-1) and (-1,0) Bloch-SPP modes can achieve  $\alpha = 0^\circ \rightarrow \beta = 90^\circ$  (figure 14D) and  $\alpha = 90^\circ \rightarrow \beta = 0^\circ$  (figure 14E) polarization conversion.

Several trends observed in figures 14C-F will be further investigated through numerical simulations in chapter 4. In section 4.3 we investigate the trends related to incident light polarization. Specifically, we use near field simulations at the locations denoted by triangles in figure 14B to explain why the (0,-1) Bloch-SPP mode shows limited transmission in figure 14C, why the (-1,0) Bloch-SPP mode shows limited transmission in figure 14F, and why both Bloch-SPP modes mediate polarization conversion. In section 4.4 we investigate the trends related to angle of incidence. Specifically, we use near field simulations at the locations indicated by circles in figure 14B to explain why the transmission in figure 14D-E along the (0,-1) Bloch-SPP mode decreases along its dispersion curve (as angle of incidence increases) and similarly why in figure 14F the transmission along the (-1,0) Bloch-SPP mode decreases along its dispersion curve. While the trends in the multi-mode regime transmission are more intricate, the essential features such as why the multi-mode regime supports polarization conversion can be described by the simple extension to our single-mode regime model presented in section 2.4. In chapter 4.6

we provide a qualitative model to explain why polarization conversion is present in the multi-mode regime, and use near field simulations at the location denoted by a square in figure 14B to support the model.

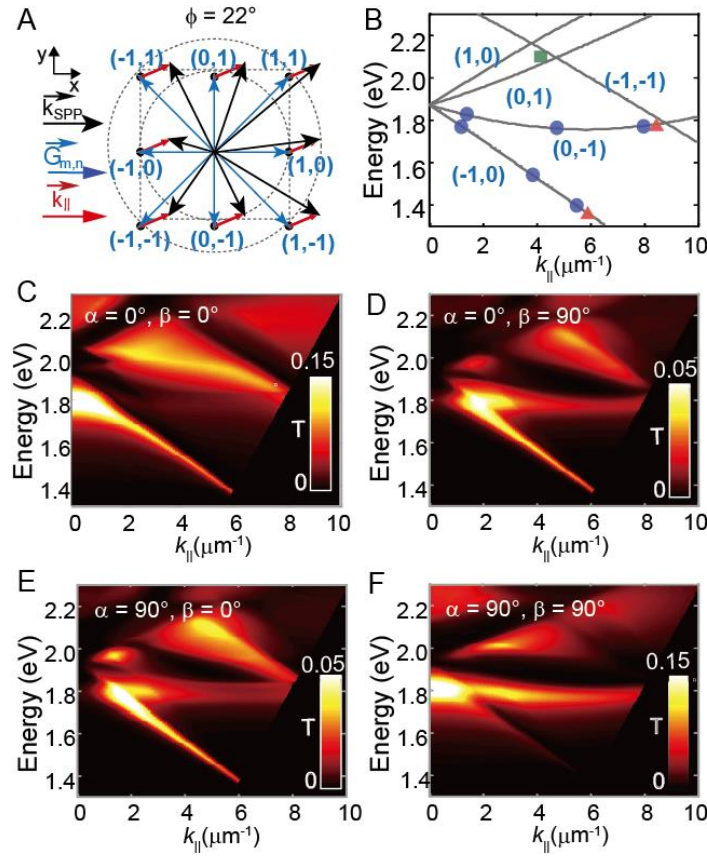


Figure 14. Experimentally Observed Extraordinary Optical Transmission for  $\phi=22^\circ$

(A) Schematic illustration of incident light with in plane wavevector  $\vec{k}_{\parallel}$  coupling to  $(m,n)$  first order Grating vector modes resulting in the excitation of the  $(m,n)$  Bloch-SPP mode when  $\phi = 22^\circ$ . (B) Plot of the dispersion relations of each Bloch-SPP mode. The triangles, circles, and square denote locations on the dispersion curves that are referenced in figure 4, 5, and 6 respectively. (C-F) Experimentally observed transmission with the azimuthal angle set to  $\phi = 22^\circ$ , the angle of incidence  $\theta$  is swept from 0 to 40 degrees, and the analyzer and polarizer directions  $(\alpha, \beta)$  are set to  $(0^\circ, 0^\circ)$  (figure 14C),  $(0^\circ, 90^\circ)$  (figure 14D),  $(90^\circ, 0^\circ)$  (figure 14E),  $(90^\circ, 90^\circ)$  (figure 14F).

### 3.5. Conclusions

The key observation from figure 14 is that by breaking the symmetry between the

incident light wavevectors and the axes of the nanohole array (defining the direction of the Grating vector directions), we are able to excite Bloch-SPPs with light that is not directly parallel to the Bloch-SPP propagation direction. Since the polarization of the transmitted light aligns with the direction of Bloch-SPP wavevectors which in general is not the same as the direction of the incident light polarization, the polarization of the transmitted light does not match that of the incident light, leading to polarization conversion.

## Chapter 4. Numerical Results – Analyzing EOT Polarization

### Conversion

While the experiments reveal interesting phenomena such as polarization conversion in EOT, the experiments only allow us to probe the far field. According to our conceptual model, much of the physics underlying these far field phenomena occurs in the near field. As the near field cannot be probed efficiently experimentally, we turn to numerical simulations to probe the near field.

To validate the simulations, we first compare the far field results obtained numerically to those obtained experimentally and observe that the simulations capture all essential features of the experiments (section 4.2). We then use the near field simulation data to tie the key trends observed experimentally in section 3.4 to the underlying physics described by our model. Specifically, the effects of the incident light polarization and incident light angle of incidence on the charge distributions are discussed in sections 4.3 and 4.4 respectively. We briefly investigate the role of film thickness and the relationship between the Bloch-SPPs observed on the front interface of the metal to those observed on the back interface of the metal (section 4.5). We then discuss EOT due to multiple Bloch-SPPs modes hybridizing (section 4.6). Finally, we discuss limitations of the simulations and identify what types of features these simulations would not be able to capture (section 4.7).

#### 4.1. Numerical Set-up

The numerical simulations were performed in “Lumerical FDTD” software. This finite difference time domain solver allows the user to define a mesh, with every mesh point attributed

a complex valued dielectric function (corresponding to the material at that point). The user also needs to define a source and boundary conditions, which the program uses to solve Maxwell's equations throughout the mesh. Finally, the user can define monitors throughout the geometry, where quantities such as electric field components and charge densities can be evaluated. Table 2 summarizes the key attributes of the Lumerical FDTD simulations used to obtain the near field charge distribution plots shown throughout this section. Figure 15 displays the user interface for a typical simulation.

*Table 2. Lumerical FDTD simulation parameters*

Lumerical FDTD Parameter	Parameter Value
Source – Wavelength	400nm to 800nm, in 2nm increments
Source – Angle of Incidence	Between 0 to 40 degrees, depending on simulation
Source – Azimuthal Angle	Either 0 or 22 degrees, depending on simulation
Source – Polarization Angle	Between 0 to 180 degrees, depending on simulation
Mesh Size	5nm on nanohole surface, up to 20nm far from nanohole surface
Materials	Ag – CRC for the thin film; dielectric with $n=1.5$ everywhere else
Film Geometry	100nm diameter holes with periodicity of 400nm. Film is 100nm thick.
Boundary Conditions	Bloch periodic (modeling an infinite array)

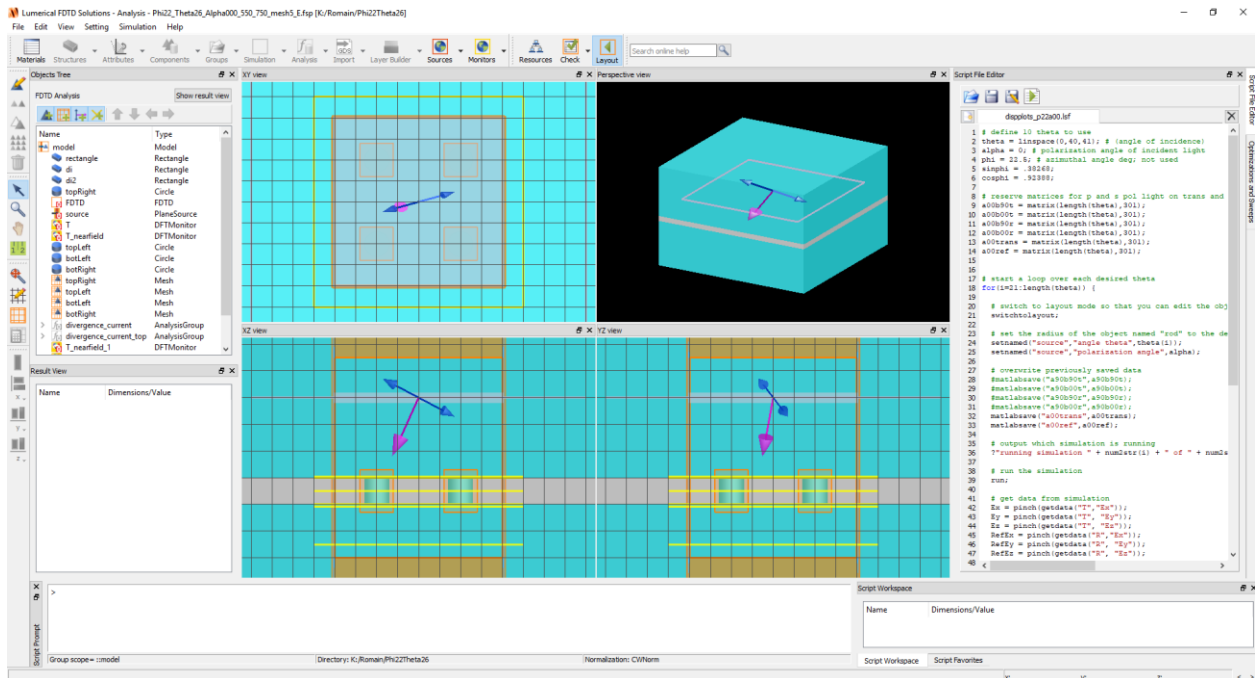


Figure 15. Typical user interface of Lumerical FDTD simulations.

## 4.2. Reproducing Experimental Results

The first set of simulations performed aim to replicate in simulation the experimental far field transmission measurements. Using the simulation parameters outlined in section 4.1, sections 4.2.1 and 4.2.2 present the simulated far field transmission data for the  $\phi = 0^\circ$  and  $\phi = 22^\circ$  experiments and highlight the strong consistency between the simulated and experimental data.

### 4.2.1. Simulating $\phi = 0^\circ$ Experiment

The Lumerical FDTD and Matlab scripts shown in Appendix 1 are used to generate the simulated dispersion plots, shown below (figures 16A and 16B). These two plots (for incident polarization along the x direction and along the y direction, respectively) show a high level of similitude to the experimentally obtained dispersion plots, capturing all essential features such as

the resonant energy of each Bloch-SPP mode (tabulated in table 3) and the degree of excitation of each Bloch-SPP mode. These plots confirm that in the far field the simulations match the experiments, and therefore the near field results from these simulations can be used to probe the physics underlying the experimentally observed phenomena (polarization conversion) presented in chapter 3.

Based on these dispersion plots, distinct regions of EOT are identified and categorized into either single mode EOT or multi-mode EOT as shown in table 4. The single-mode EOT is completely captured by the model presented in chapter 2, and the near field results corresponding to the transmission in this regime are thoroughly analyzed in sections 4.3-4.5. The qualitative discussion of multi-mode EOT, including a presentation of the different types of multi-mode EOT, is provided in section 4.6.

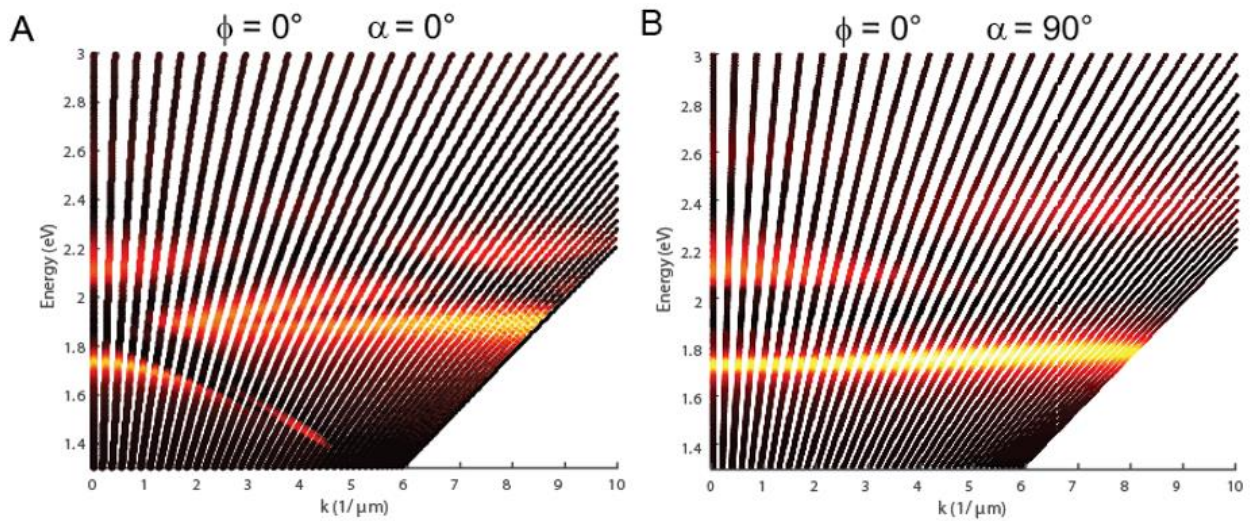


Figure 16. Simulated transmission for  $\phi = 0^\circ$ .

(A-B) Total transmission intensity measured in Lumerical FDTD simulations when the azimuthal angle  $\phi$  and the incident light polarization  $\alpha$  are set to  $\phi = 0^\circ, \alpha = 0^\circ$  (A),  $\phi = 0^\circ, \alpha = 90^\circ$  (B).

Table 3. Analytically expected first order resonances for  $\phi=0^\circ$

$\theta$ (in $^\circ$ )	(-1,0) Bloch-SPP mode	(0,+1) Bloch-SPP modes	(1,0) Bloch-SPP mode
5	1.75eV or 708nm	1.90eV or 652nm	2.0eV or 619nm
18	1.60eV or 775nm	2.05eV or 605nm	2.4eV or 517nm
26	1.50eV or 826nm	2.15eV or 577nm	N/A

Table 4. Simulated  $\phi=0^\circ$  - Categorizing single-mode EOT and multi-mode EOT

$\theta$ (in $^\circ$ )	Simulated EOT region 1			Simulated EOT region 2		
	Resonant Energy	Bloch-SPP Modes Involved	Categorization of EOT	Resonant Energy	Bloch-SPP Modes Involved	Categorization of EOT
5	1.75eV	(-1,0)	Single-mode	2.2eV	(1,0), (-1,+1)	Multi-mode Hybridized
18	1.60eV	(-1,0)	Single-mode	2.05eV	(0,+1)	Multi-mode Hybridized
26	1.45eV	(-1,0)	Single-mode	2.00eV, 2.20eV	(0,+1), (-1,+1)	Multi-mode Hybridized

#### 4.2.2. Simulating $\phi = 22^\circ$ Experiment

Figures 17C and 17D are produced analogously to those in section 4.2.1, but with the azimuthal angle set to  $\phi = 22^\circ$ . As in section 4.2.1, these plots agree with the experimentally measured dispersion plots. Table 5 displays key features of the dispersion plots and table 6 displays categorization of each measured resonance.

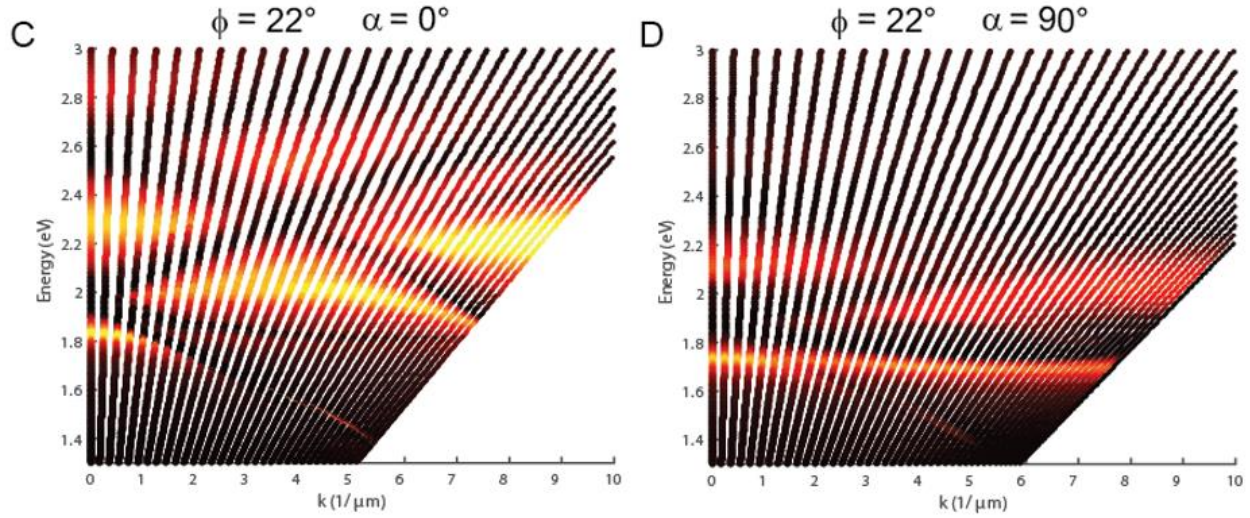


Figure 17. Simulated transmission for  $\phi = 22^\circ$

(C-D) Total transmission intensity measured in Lumerical FDTD simulations when the azimuthal angle  $\phi$  and the incident light polarization  $\alpha$  are set to  $\phi = 22^\circ, \alpha = 0^\circ$  (C), and  $\phi = 22^\circ, \alpha = 90^\circ$  (D).

Table 5. Analytically expected first order resonances for  $\phi = 22^\circ$

$\theta$ (in $^\circ$ )	(-1,0) Bloch-SPP mode	(0,-1) Bloch-SPP mode	(0,1) Bloch-SPP mode	(1,0) Bloch-SPP mode
2	1.85eV	1.90eV	1.90eV	1.95eV
8	1.80eV	1.85eV	1.95eV	2.00eV
12	1.60eV	1.80eV	2.05eV	2.20eV
18	1.50eV	1.75eV	2.20eV	2.45eV
26	1.40eV	1.75eV	2.35eV	N/A

Table 6. Simulated  $\phi = 22^\circ$  - Categorizing single-mode EOT and multi-mode EOT

$\theta$ (in $^\circ$ )	Single-Mode Simulated EOT	Multi-Mode Simulated EOT

	Resonant Energy	Bloch-SPP Modes Involved	Categorization of EOT	Resonant Energy	Bloch-SPP Modes Involved	Categorization of EOT
2	1.80eV; 1.80eV	(-1,0); (0,-1)	Single-mode	2.2eV	(1,0), (-1,+1)	Multi-mode Hybridized
8	1.75eV; 1.80eV	(-1,0); (0,-1)	Single-mode	1.95eV	(0,+1), (1,0), (-1,-1)	Multi-mode Hybridized
12	1.70eV; 1.80eV	(-1,0); (0,-1)	Single-mode	1.95eV	(0,+1), (1,0), (-1,-1)	Multi-mode Hybridized
18	1.6eV; 1.80eV	(-1,0); (0,-1)	Single-mode	1.90eV	(0,+1), (1,0), (-1,-1)	Multi-mode Hybridized
26	1.5eV; 1.80eV	(-1,0); (0,-1)	Single-mode	1.90eV; 2.10eV	(0,+1), (1,0), (-1,-1) (-1,-1), (1,0), (0,1), (0,-1)	Multi-mode Hybridized Multi-mode Hybridized

### 4.3. Role of Incident Light Polarization

To verify the role of incident light polarization on Bloch-SPP excitation and the associated EOT measured in figure 14, we experimentally measure transmission intensity for the configuration  $\phi = 22^\circ, \theta = 40^\circ$  over a wavelength range that includes the resonant wavelengths for the (-1,0) and the (0,-1) Bloch-SPP modes as the incident polarization angle is swept from  $0^\circ$  to  $180^\circ$ , as shown in figure 18A. Figures 18B and 18C display slices of this data at the resonance wavelength for the (0,-1) Bloch-SPP mode (corresponding to the upper triangle in figure 14B) and (-1,0) Bloch-SPP mode (corresponding to the lower triangle in figure 14B) respectively.

These figures show that the total transmitted intensity (shown by black dots), which is proportional to Bloch-SPP excitation and therefore coupling efficiency, follows the  $\cos^2(\alpha_{\parallel} - \rho)$  dependence predicted by equation (2.1) (solid black line) with peak positions consistent with  $\alpha_{optimal}$  values predicted by equation (2.15) for this geometrical set-up:  $24.8^\circ$  for the (-1,0) Bloch-SPP mode and  $98.9^\circ$  for the (0,-1) Bloch-SPP mode.

To tie the far field experimental results to the near field physics, figure 18D-L investigate the near field charge distributions from the simulations used to provide the far field data presented in figure 18A-C. Figure 18E-H, taken at the resonant wavelength for the (0,-1) Bloch-SPP mode, show that the incident polarization dependence of Bloch-SPP excitation matches the incident polarization dependence of the far field transmission intensity: optimal excitation near  $\alpha = \alpha_{optimal}$  (figure 18G) and decaying as  $\cos^2(\alpha_{\parallel} - \rho)$  away from this optimal polarization. Figure 18I-L show that the Bloch-SPP excitation for the (-1,0) Bloch-SPP mode also follows this behavior.

These results bring physical justification to our model's prediction (see equation 2.17) that at the location denoted by the triangle in figure 14B the (-1,0) mode should show least transmission in figure 14F, more transmission in figures 14D and 14E (by equation 2.17, the transmission in 14D-E should be greater than that in 14F by a factor of 4.6), and finally the most transmission in figure 14C (by equation 2.17, the transmission in 14C should be greater than that in 14D-E by a factor of 3.8). Similarly, these figures justify our model's prediction that the (0,-1) Bloch-SPP mode should show limited transmission in figure 14C, but still mediate polarization conversion in figure 14D and 14E.

The red and blue lines in figure 18B and 18C, representing the measured transmittance decomposed into its p-polarized (blue lines) and s-polarized (red lines) components, allow us to

also verify the coupling-out process. In the case of the  $(-1,0)$  Bloch-SPP mode, equation (2.2) yields  $\rho = 171.5^\circ$ , meaning that the ratio of transmitted light intensity measured in the  $\beta = 0^\circ$  polarization to that in the  $\beta = 90^\circ$  direction by equation (2.16) should be  $\frac{\cos^2(0+\phi-\rho)}{\cos^2(90+\phi-\rho)} = 2.77$ . This is consistent with figure 18C showing the blue line approximately 2.75 times higher than the red line. In the case of the  $(0,-1)$  Bloch-SPP mode, equation (2.2) yields  $\rho = 111.1^\circ$  suggesting that the ratio of transmitted light intensity measured in the  $\beta = 0^\circ$  polarization direction to that in the  $\beta = 90^\circ$  direction should be .000686. This is consistent with the experimental results in figure 18B showing the red line significantly higher than the blue line.

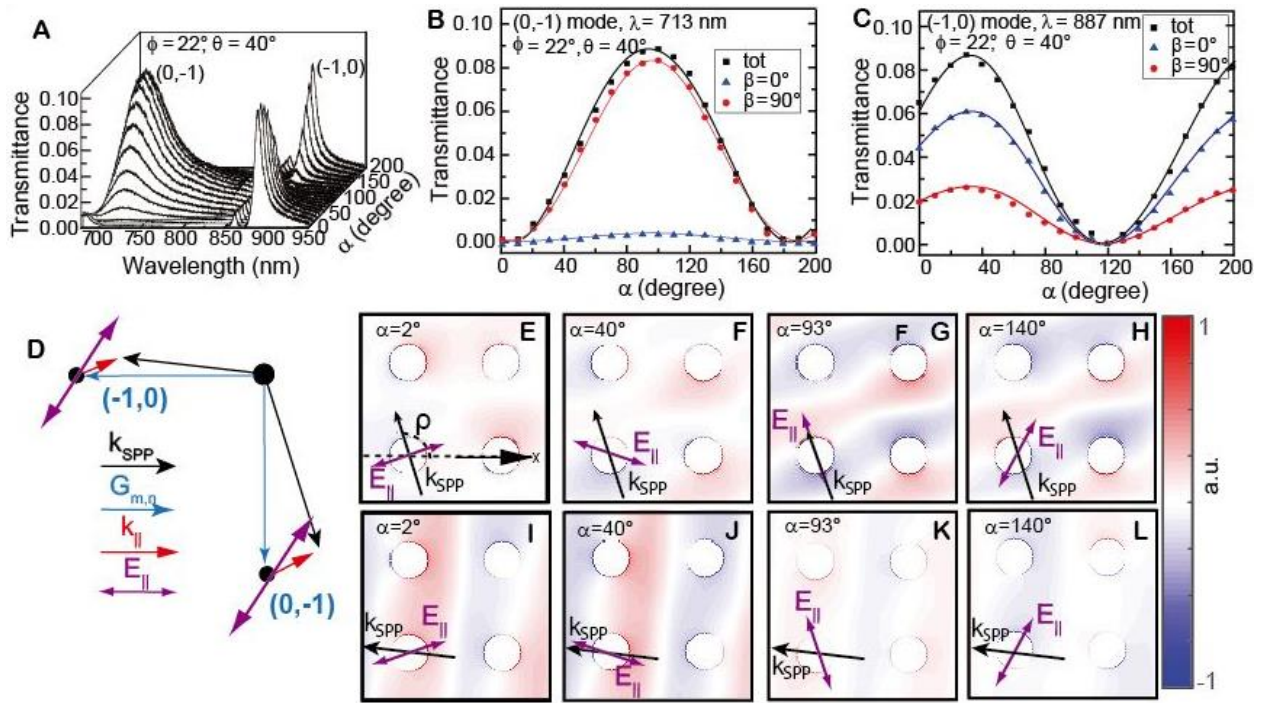


Figure 18. Importance of Incident Polarization in Bloch-SPP Excitation and EOT.

(A) Simulated (FDTD as described in methods) total transmission measured from 700nm-950nm, with the azimuthal angle and angle of incidence set to  $\phi = 22^\circ, \theta = 40^\circ$ , and repeated for various incident polarization angles. (B-C) Transmission at the  $(0,-1)$  Bloch-SPP mode resonant wavelength  $\lambda = 713\text{nm}$  (B) and at the  $(-1,0)$  Bloch-SPP mode resonant wavelength  $\lambda = 887\text{nm}$  (C) for various incident polarization angles. Simulated total transmission shown by black dots, transmission passing through a  $\beta = 0^\circ$  polarizer shown by blue dots, and

transmission passing through a  $\beta = 90^\circ$  polarizer shown by red dots. Solid lines show  $\cos^2(\alpha_{||} - \rho)$  fits to the simulated data. (D) Schematic illustration of expected propagation directions of (-1,0) and (0,-1) Bloch-SPP modes for  $\phi = 22^\circ, \theta = 40^\circ$  and incident polarization is varied. (E-H) Simulated near field charge distribution on the front metal-dielectric interface for  $\phi = 22^\circ, \theta = 40^\circ$ , evaluated at 713nm, with  $\alpha = 2^\circ$  (E),  $\alpha = 40^\circ$  (F),  $\alpha = 93^\circ$  (G),  $\alpha = 140^\circ$  (H). (I-L) Simulated near field charge distribution on the front metal-dielectric interface for  $\phi = 22^\circ, \theta = 40^\circ$ , evaluated at 887nm, with  $\alpha = 2^\circ$  (I),  $\alpha = 40^\circ$  (J),  $\alpha = 93^\circ$  (K),  $\alpha = 140^\circ$  (L).

#### 4.4. Role of Angle of Incidence

Another trend observed in figure 3 in single mode regime transmission is that the intensity of the transmission mediated by a given Bloch-SPP mode changes along the mode's dispersion curve. In other words, the coupling-in and coupling-out processes associated with a given Bloch-SPP mode depend on the angle of incidence. While equation (2.2) and figures 18E-L show that the direction of the Bloch-SPP wavevector cannot be changed by sweeping the incident polarization angle, the direction of the Bloch-SPP wavevector can be changed by varying the angle of incidence, as shown in figure 19A-B. As the Bloch-SPP propagation direction changes,  $\alpha_{opt}$  varies (equation 2.15), thereby varying the coupling-in efficiency according to equation (2.1). This trend can be seen by the varying charge distribution intensities shown in figures 19C-E for the (0,-1) Bloch-SPP mode and in figures 19F-H for the (-1,0) Bloch-SPP mode (corresponding to the circles in figure 14B). In addition to the coupling-in process being affected, the coupling-out process is also affected as the direction of the transmitted light polarization changes (equation 2.2), and so the polarization conversion efficiency will vary according to equation (2.17). Figure 19I compares the  $\alpha = 0^\circ \rightarrow \beta = 90^\circ$  polarization conversion efficiency predicted by equation (2.17) (solid red line) to the transmission experimentally observed in figure 14 (red dots) for light mediated by the (0,-1) Bloch-SPP mode. The  $\alpha = 0^\circ \rightarrow \beta = 0^\circ$  transmission efficiency predicted by equation (2.17) (solid blue line) is

also compared to the transmission experimentally observed in figure 14 (blue dots). Figure 19J shows that this consistency also holds for light transmitted by the (-1,0) Bloch-SPP mode. The consistency between the analytically predicted polarization conversion efficiency and the experimental results directly supports equation (2.17).

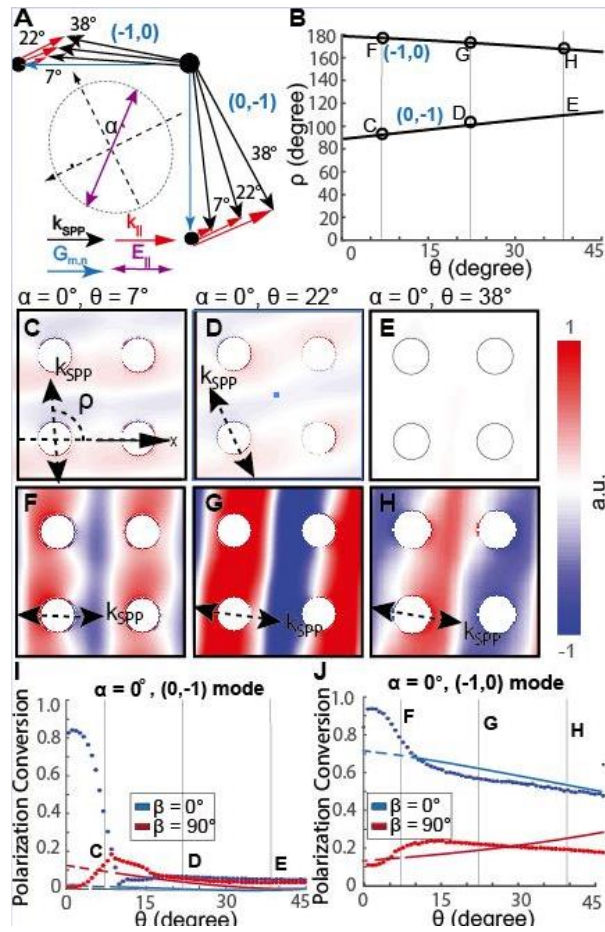


Figure 19. Importance of Angle of Incidence in Bloch-SPP Excitation and EOT

(A) Schematic illustration of expected propagation directions of (-1,0) and (0,-1) Bloch-SPP modes with the azimuthal angle  $\phi = 22^\circ$  and the angle of incidence  $\theta$  being varied. (B) Bloch-SPP propagation direction  $\rho$  as a function of incidence angle  $\theta$  for the (-1,0) and (0,-1) Bloch-SPP modes as given by equation (2.2) (solid black lines) and extracted from the near field simulation data shown in figure (C)-(H) (black circles). (C-H) Near field charge distribution map evaluated at the front metal-dielectric interface with incident light polarization  $\alpha = 0^\circ$  at the wavelength corresponding to the (0,-1) Bloch-SPP mode resonance (C-E) and to the (-1,0) Bloch-SPP mode resonance (F-H) with the angle of incidence set to  $\theta = 7^\circ$  (C,F),  $\theta = 22^\circ$  (D,G), and  $\theta = 38^\circ$  (E,H). The Bloch-SPP propagation direction extracted from these figures is represented by the black

arrow. (I-J) Polarization conversion efficiency as a function of incidence angle when incident polarization angle is set to  $\alpha = 0^\circ$  for the (0,-1) Bloch-SPP mode (I) and the (-1,0) Bloch-SPP mode (J). The solid blue (red) line shows the analytically expected intensity of the light transmitted by the (0,-1) Bloch-SPP mode after passing through a  $\beta = 0^\circ$  ( $\beta = 90^\circ$ ) polarizer, obtained from equation (4). Dotted blue (red) line shows transmission experimentally observed along the (0,-1) Bloch-SPP mode in figure 14C (figure 14D). Note that the single mode regime is not valid for angle of incidences less than  $\theta = 10^\circ$ , and therefore we do not expect our single mode regime model to match the experimental data in this regime.

#### 4.5. Coupling between Bloch-SPPs on Front and Back Surfaces of Nanohole Array

This section aims to provide numerical evidence to support the claim that the same Bloch-SPP mode that is excited on the front surface of the nanohole array by the incident light will also be present on the back surface of the nanohole array.

The conceptual model explains that due to evanescent coupling through the nanohole array, Bloch-SPPs will be formed on the back surface of the nanohole array with the same propagation direction as those on the front surface of the nanohole array. In this section we show that this is supported by numerical simulations, as for various film thicknesses the same Bloch-SPP modes are observed on the front and back surfaces.

Figure 20A shows the momentum diagram for the two Bloch-SPP modes analyzed in figure 18: the (0,-1) and (-1,0) Bloch-SPP modes when the azimuthal angle is set to  $\phi = 22^\circ$  and the angle of incidence is set to  $\theta = 40^\circ$ . Figures 20B and 20C show the charge density distribution at the wavelength associated with the (0,-1) Bloch-SPP mode on the front and back surface of the nanohole array respectively for various incident light polarizations. As can be seen from these figures, regardless of the incident light polarization, the charge distribution pattern on the front and back surfaces are the same, modulo a phase factor. The incident light polarization

serves only to determine the extent of the Bloch-SPP excitation, as in explained in figure 18.

Figures 20C and 20D show the analogous plots for the (-1,0) Bloch-SPP mode.

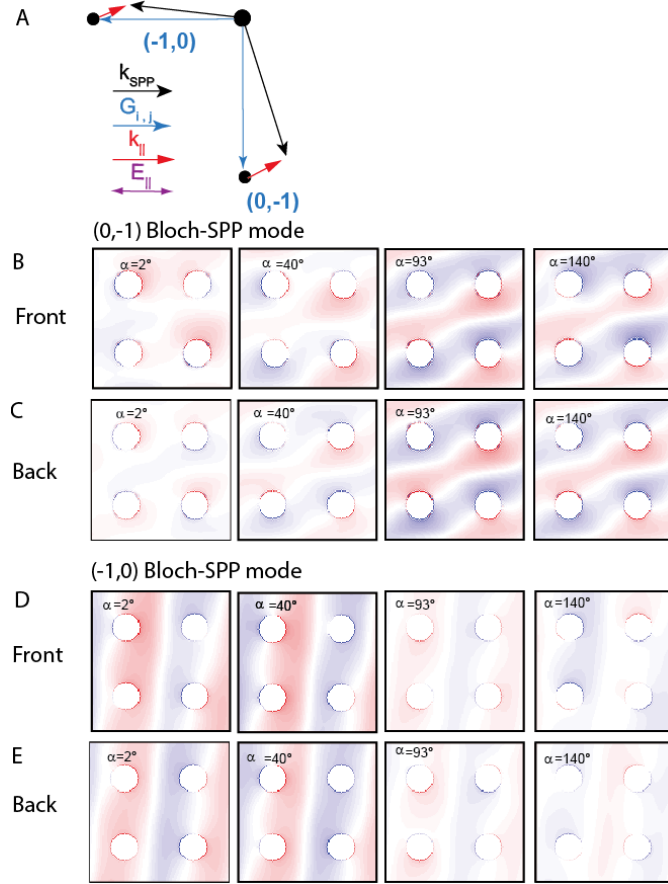


Figure 20. Comparison of Bloch-SPPs on front and back surfaces of nanohole array

(A) k-space schematic representing the (-1,0) and (0,-1) Bloch-SPP modes. (B-C) Charge distribution plots for various polarizations on the front (B) and backs (C) surfaces of the nanohole array at the (0,-1) Bloch-SPP mode resonance. (D-E) Charge distribution plots for various polarizations on the front (D) and backs (E) surfaces of the nanohole array at the (-1,0) Bloch-SPP mode resonance.

#### 4.6. Analysis of Multi-Mode Regime

Section 2.4 identified that in the multi-mode regime, standing waves formed from interference between pairs of excited Bloch-SPP modes dominate the dipole direction of each nanohole. To investigate this model, numerical simulations were performed with the azimuthal

angle set to  $\phi = 22^\circ$ , angle of incidence set to  $\theta = 12^\circ$ , and the incident light wavelength set to  $\lambda = 575\text{nm}$ , at which configuration the (1,0), (0,1), and (-1,-1) Bloch-SPP modes are all simultaneously excited.

Figures 21A-C show the standing waves formed in this configuration, and figure 21D summarizes the three resulting dipole directions. In figures 21E and 21H, the incident light polarization is set such that  $\vec{E}_{\parallel}$  is parallel to the blue standing wave, and therefore the overall dipole direction of each nanohole is in the direction of the blue standing wave (shown in figure 21B). Analogously, figures 21G and 21J illustrate a case in which the incident light polarization is set such that the dipole direction of each nanohole is in the direction of the red standing wave (shown in figure 21A). In figures 21F and 21I, the incident light polarization is non-orthogonal to each standing wave direction, and therefore the overall dipole direction is given by a superposition of all three dipole directions. As the overall dipole direction, which determines the polarization of the transmitted light, is given by a combination of multiple standing waves which in general is not parallel to the incident light polarization, this model successfully explains the microscopic origin of the polarization conversion observed in multi-mode regime EOT (figure 14).

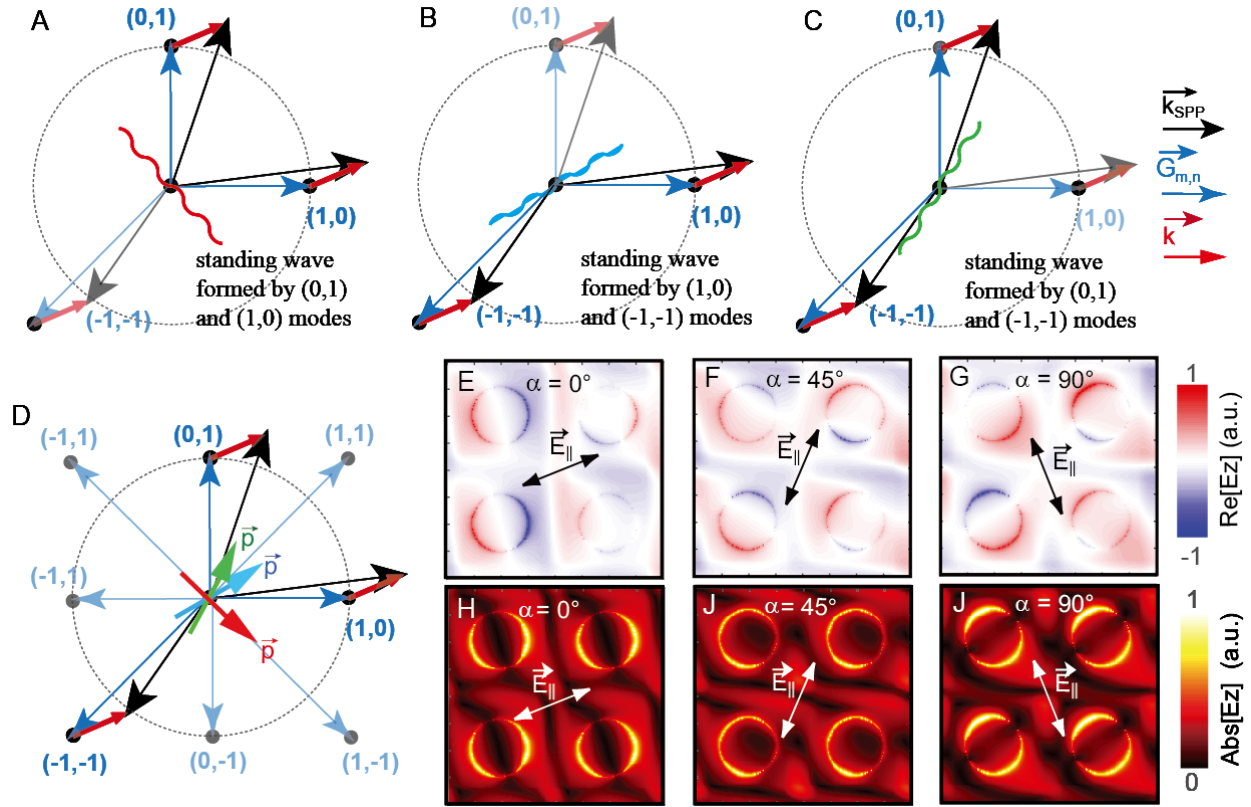


Figure 21. Multi-mode regime – hybridized Bloch-SPP mode case.

(A) Schematic illustration of the standing wave formed by the interference of the (0,1) and (1,0) Bloch-SPP modes. (B) Standing wave formed by (1,0) and (-1,-1) Bloch-SPP modes. (C) Standing wave due to (0,1) and (-1,-1) Bloch-SPP modes. (D) Summary of the three standing wave directions that can be excited with an efficiency determined by the incident light polarization. (E-G) Real part of z component of electric field on the front surface of the nanohole array at 575nm when the incident light polarization is set to  $\alpha = 0^\circ$  (E),  $\alpha = 45^\circ$  (F), and  $\alpha = 90^\circ$  (G). (H-J) Absolute value of the z component of electric field on the front surface of the nanohole array at 575nm when the incident light polarization is set to  $\alpha = 0^\circ$  (H),  $\alpha = 45^\circ$  (I), and  $\alpha = 90^\circ$  (J). The contribution of each standing wave to the overall dipole direction of each nanohole depends on the angle between the standing wave direction and the incident light in-plane electric field direction.

## 4.7. Limitations of Simulations

While FDTD simulations capture most of the essential phenomena, as evidenced by the similitude between the experimental and numerical dispersion plots, it is important to discuss ways in which the simulations are not perfect.

One limitation of Lumerical FDTD is that only discrete set of wavelengths are probed, so if resonance maximum occurs between two wavelength points, the maximum resonance from the simulation underestimates the true maximum resonance. This means we cannot fully trust relative resonance excitations, especially for narrow resonances (wavelength sampling is 2nm, so for resonances with strong gradients over 2nm).

Secondly, quantum mechanical effects are not captured by Lumerical FDTD. We do not expect any significant contribution from quantum mechanical effects, and our model assume no quantum mechanical effects, so this limitation is acceptable.

## Chapter 5. Conclusions and Outlook

A summary of the key insights developed in this work is presented in section 5.1. Section 5.2 outlines the current applications of EOT and polarization conversion, and comments on how the key insights from this work may affect these applications. Finally, section 5.3 suggests future work that would complement this study.

### 5.1. Key Insights

The principle achievement of this work is to present a microscopic model of SPP excitation and SPP mediated EOT. In the single mode regime, this work describes a quantitative way of determining the extent to which incident light can excite a given SPP mode, based on the incident light polarization. In the multi-mode regime, this work presents the first description of the microscopic behavior of hybridized SPP modes. This conceptual picture highlighting the importance of surface effects will help the field understand other surface waves, such as surface acoustic waves, which have found growing importance in diverse applications such as quantum computing, acting as an interface for entangling qubits.

The secondary achievement of this work has been the proof-of-concept demonstration of a new approach to achieving polarization conversion. While current polarization conversion is typically achieved through chiral nanoholes, and thus depends heavily on the fabrication quality of each nanohole, in this work polarization conversion is achieved by nonlocal Bloch-SPPs, and as such is robust to fabrication imperfections. This could have significant impact on applications necessitating polarization conversion, as explained in section 5.2.

## 5.2. Potential Applications

EOT and polarization conversion are utilized in many applications including filtering and switching<sup>24</sup>, nonlinear optics<sup>12,40</sup>, surface plasmon resonance sensing<sup>12-14,33,41,42</sup>, surface enhanced fluorescence<sup>12</sup>, surface-enhanced Raman scattering<sup>12</sup>, and absorption spectroscopy<sup>12</sup>. The potential impact of this work will be discussed for two of these applications explicitly, but similar impacts are expected in the other applications.

One straightforward application of this work is in the use of polarization division multiplexing, or using polarization of light to send multiple signals across one communication channel, to increase the transmission capacity of optical fibers. In 2013, Mandal et al reported an experiment constituting an H-shaped nanohole which supported transmission at two distinct wavelengths with orthogonal polarizations. The incident light polarization determined whether the transmitted light was at the first wavelength, the second wavelength, or a linear combination of both wavelengths: “flipping the stat from linear-x to linear-y switches the transmission from near infrared to visible resonance wavelength demonstrating the use as a demultiplexer [device for multi-input multi-output (MIMO) schemes]”<sup>24</sup>. The nanohole array in this work is also capable of supporting two orthogonal transmission resonances with orthogonal polarizations: when the azimuthal angle is set to  $\phi = 22^\circ$  and the angle of incidence is set to  $\theta = 10^\circ$ , the (-1,0) and (0,-1) Bloch-SPP modes have nearly orthogonal polarizations and resonant wavelengths of 776nm and 690nm respectively. There are two advantages to using nanohole arrays rather than the H-shaped nanohole currently used: (1) the polarization effects are more robust to fabrication imperfections; (2) the nanohole array provides more flexibility for future extension. Regarding fabrication imperfections, the polarization conversion in H-shaped nanoholes occurs locally at the nanohole, meaning that the phenomenon is extremely sensitive to the shape of the

nanohole. In contrast, polarization conversion through nanohole arrays is due to the propagation direction of the Bloch-SPPs, which only necessitates some periodic potential across the array, but does not depend on the specific shape of each nanohole. Therefore, the nanohole array is expected to be more robust against fabrication imperfections than the H-shaped nanohole, though future experiments should test this experimentally. Perhaps more interestingly, nanohole arrays support multiple Bloch-SPP modes with distinct energy, each with its own (analytically evaluable) polarization direction. For example, when the azimuthal angle is set to  $\phi = 22^\circ$  and the angle of incidence is set to  $\theta = 10^\circ$ , each of the (0,1), (1,0), (0,-1), and (-1,0) modes are individually accessible, allowing a four way demultiplexer, compared to the H-shaped nanohole which only supports two modes.

Another potential application is in biomedical sensing using a technique known as surface plasmon resonance (SPR). Traditional SPR indicates the presence of biomolecules and their binding by measuring minute refractive index variations along the surface of a metal film which shift the wavelengths of the surface plasmon resonances<sup>13</sup>. The dependence of the wavelength of surface plasmon resonance on the surrounding medium can be understood through the derivation in section 1.2.1, specifically equation 1.7. One limitation of this technique is that the broadness of surface plasmon transmission peaks leads to a low signal-to-noise ratio. The understanding of the role of incident light polarization presented in this paper could provide a new approach to improving the signal-to-noise ratio in the measured transmission. Instead of shining unpolarized light to excite the SPR, a polarizer could be placed between the incident light source and the sample. The transmission spectrum could be measured as the polarizer is rotated. Based on the model developed in this paper, the transmission spectrum should show that the intensity of the SPR transmission peak has a cosine squared dependence on the incident light

polarization, with a maximum intensity when the incident light polarizer is set to some angle  $\alpha_0$  (which can be calculated analytically following the procedure outline in section 2.1.1). If the polarizer is set 90 degrees away from  $\alpha_0$ , we know that the SPR should not be excited at all, which means any residual transmission can be categorized as noise (either from a different SPR resonance, from some other form of scattering, etc). This noise can then be subtracted from the spectrum obtained when the incident light polarizer is set to  $\alpha_0$ , thereby improving the signal-to-noise ratio.

In summary, the model developed in this work opens a new degree of freedom (SPP polarization) which can be used to tackle existing obstacles in new ways in a diverse set of applications.

### 5.3. Future Work

The fundamental model proposed in this work could be further verified from a variety of approaches. For example, a different geometry of holes could be considered, such as a periodic triangular lattice. By changing the real space lattice in such a way, the reciprocal space lattice would also change, and thus the Grating vectors available to bridge the momentum mismatch between free space light and SPPs would change. Even within the square lattice studied in this work, changing the periodicity from 400nm to 800nm would halve the magnitude of the Grating vectors, thereby increasing the importance of the incident light in-plane momentum in determining the direction of the Bloch-SPPs. Collecting analogous data to that presented in this study for a new geometry would provide a different testbed to verify our model.

Much of the future work could be focused on incorporating the new understanding of the role of SPPs in EOT and in polarization conversion to applications. While approaches to incorporating nanohole arrays into optical elements and into biomedical sensing were outlined in the section 5.2, the new understanding of SPPs should allow developments in a multitude of different applications such as non-linear optics and energy harvesting.

## References

- (1) Ebbesen, T. W.; Lezec, H. J.; Ghaemi, H. F.; Thio, T.; Wolff, P. A. Extraordinary Optical Transmission through Sub-Wavelength Hole Arrays. *Nature* **1998**, *391*.
- (2) Ghaemi, H., Thio, T., Grupp, D., Ebbesen, T., Lezec, H. Surface Plasmons Enhance Optical Transmission through Subwavelength Holes. *Phys. Rev. B* **1998**.
- (3) Martin-Moreno, L., Garcia-Vidal, F., Lezec, H., Pellerin, K., Thio, T., Pendry, J., Ebbesen, T. Theory of Extraordinary Optical Transmission through Subwavelength Holes Arrays. *Phys. Rev. Lett.* **2001**.
- (4) Krishnan, A.; Thio, T.; Kim, T. J.; Lezec, H. J.; Ebbesen, T. W.; Wolff, P. A.; Pendry, J.; Martin-Moreno, L.; Garcia-Vidal, F. J. Evanescently Coupled Resonance in Surface Plasmon Enhanced Transmission. *Opt. Commun.* **2001**.
- (5) Enoch, S., Popov, E., Neviere, M., Reinisch, R. Enhanced Light Transmission by Hole Arrays. *J. Opt. Pure Appl. Opt.* **2002**.
- (6) Andrew, P. Energy Transfer Across a Metal Film Mediated by Surface Plasmon Polaritons. *Science (80-. )*. **2004**, *306*, 1002–1005.
- (7) Barnes, W. L.; Murray, W. A.; Dintinger, J.; Devaux, E.; Ebbesen, T. W. Surface Plasmon Polaritons and Their Role in the Enhanced Transmission of Light Through Periodic Arrays of Subwavelength Holes in a Metal Film. *Phys. Rev. Lett.* **2004**.
- (8) Gao, H.; Henzie, J.; Odom, T. W. Direct Evidence for Surface Plasmon-Mediated Enhanced Light Transmission through Metallic Nanohole Arrays. *Nano Lett.* **2006**.
- (9) Liu, H.; Lalanne, P. Microscopic Theory of the Extraordinary Optical Transmission.

*Nature* **2008**.

- (10) Salomon, L., Grillot, F., Zayats, A., de Fornel, F. Near-Field Distribution of Optical Transmission of Periodic Subwavelength Holes in a Metal Film. *Phys. Rev. Lett.* **2001**.
- (11) Genet, C.; Ebbesen, T. W. Light in Tiny Holes. *Nature* **2007**.
- (12) Gordon, R.; Brolo, A. G.; Sinton, D.; Kavanagh, K. L. Resonant Optical Transmission through Hole-Arrays in Metal Films: Physics and Applications. *Laser and Photonics Reviews*, 2010.
- (13) Garcia-Vidal, F., Martin-Morena, L., Ebbesen, T., Kuipers, L. Light Passing through Subwavelength Apertures. *Rev. Mod. Phys.* **2010**.
- (14) Barnes, W. L.; Dereux, A.; Ebbesen, T. W. Surface Plasmon Subwavelength Optics. *Nature* **2003**.
- (15) Isfort, G., Schierbaum, K., Zerulla, D. Polarization Dependence of Surface Plasmon Polariton Emission. *Phys. Rev. B* **2006**.
- (16) Isfort, G.; Schierbaum, K.; Zerulla, D. Polarization Dependence of Surface Plasmon Polariton Emission.
- (17) Altewischer, E., van Exter, M., Woerdman, J. Polarization Analysis of Propagating Surface Plasmons in a Subwavelength Hole Array. *J. Opt. Soc. Am. B* **2003**.
- (18) Gordon, R.; Brolo, A. G.; McKinnon, A.; Rajora, A.; Leathem, B.; Kavanagh, K. L. Strong Polarization in the Optical Transmission through Elliptical Nanohole Arrays. *Phys. Rev. Lett.* **2004**.
- (19) Genet, C., van Exter, M., Woerdman, J. Huygens Description of Resonance Phenomena in

- Subwavelength Hole Arrays. *J. Opt. Soc. Am. A* **2005**.
- (20) Dimaiio, J. R.; Ballato, J.; Ebbesen, W.; Gripp, D. E.; Lezec, H. J. Polarization-Dependent Transmission through Subwavelength Anisotropic Aperture Arrays. *J. W. Strutt (Lord Rayleigh) Proc. R. Soc. London A Phys. Rev. B Phys. Rev. Opt. EXPRESS* **1999**, *6*, 1734–1928.
- (21) Strelniker, Y. Theory of Optical Transmission through Elliptical Nanohole Arrays. *Phys. Rev. B* **2007**.
- (22) Zhao, Q.; Li, C.; Zhou, Y.-S.; Wang, H.-Y. The Mechanism of the Polarization Dependence of the Optical Transmission in Subwavelength Metal Hole Arrays. *J. Phys. Condens. Matter* **2011**.
- (23) Romain, X., Baida, F., Boyer, P. Extended Malus Law with Terahertz Metallic Metamaterials for Sensitive Detection with Giant Tunable Quality Factor. *Phys. Rev. B* **2016**.
- (24) Mandal, P., Ramakrishna, S., Patil, R., Gopal, A. Polarization Dependent Color Switching by Extra-Ordinary Transmission in H-Slit Plasmonic Metasurface. *J. Appl. Phys.* **2013**.
- (25) Elliot, J., Smolyaninov, I., Zheludev, N., Zayats, A. Polarization Control of Optical Transmission of Elliptical Nanoholes in a Metal Film. *Opt. Lett.* **2004**.
- (26) Gordon, R., Hughes, M., Leathem, B., Kavanagh, K., Brolo, A. Basis and Lattice Polarization Mechanisms for Light Transmission through Nanohole Arrays in a Metal Film. *Nano Lett.* **2005**.
- (27) Bao, Y., Zhang, B., Wu, Z., Si, J., Wang, M., Peng, R. Surface-Plasmon-Enhanced

- Transmission through Metallic Film Perforated with Fractal Featured Aperture Array. *Appl. Phys. Lett.* **2007**.
- (28) Lovera, P.; Jones, D.; Corbett, B.; O’Riordan, A. Polarization Tunable Transmission through Plasmonic Arrays of Elliptical Nanopores. *Opt. Express* **2012**.
- (29) Wu, S.; Zhang, Z.; Zhang, Y.; Zhang, K.; Zhou, L.; Zhang, X.; Zhu, Y. Enhanced Rotation of the Polarization of a Light Beam Transmitted through a Silver Film with an Array of Perforated S-Shaped Holes. *Phys. Rev. Lett.* **2013**.
- (30) Klimov, V. V.; Zabkov, I. V.; Pavlov, A. A.; Shiu, R.-C.; Chan, H.-C.; Guo, G. Y. Manipulation of Polarization and Spatial Properties of Light Beams with Chiral Metafilms. *Opt. Express* **2016**.
- (31) Schaadt, D. M.; Feng, B.; Yu, E. T. Enhanced Semiconductor Optical Absorption via Surface Plasmon Excitation in Metal Nanoparticles Improved Performance of Amorphous Silicon Solar Cells via Scattering from Surface Plasmon Polaritons in Nearby Metallic Nanoparticles Enhanced Semiconductor Op. *Cit. Appl. Phys. Lett. J. Appl. Phys. Appl. Phys. Lett. Appl. Phys. Lett. Appl. Phys. Lett. Appl. Phys. Lett. Appl. Phys. Lett.* **2005**, *86*, 63106–93105.
- (32) Zhang, X.; Shah, N. C.; Van Duyne, R. P. Sensitive and Selective Chem/bio Sensing Based on Surface-Enhanced Raman Spectroscopy (SERS). *Vib. Spectrosc.* **2006**, *42*, 2–8.
- (33) Brolo, A., Gordon, R., Leathem, B., Kavanagh, L. Surface Plasmon Sensor Based on the Enhanced Light Transmission through Arrays of Nanoholes in Gold Films. *ACS Langmuir* **2004**.

- (34) Zhu, W.; Rukhlenko, I. D.; Xiao, F.; Premaratne, M. Polarization Conversion in U-Shaped Chiral Metamaterial with Four-Fold Symmetry Breaking. *J. Appl. Phys.* **2014**.
- (35) Bouchon, P.; Lévesque, Q.; Makhsiyan, M.; Pardo, F.; Jaeck, J.; Haïdar, R.; Pelouard, J.-L. L-Shaped Metallic Antenna for Linear Polarization Conversion in Reflection. **2015**, 937100.
- (36) Cao, Z., Yiu, L., Zhang, Z., Chan, C., Ong, H. Understanding the Role of Surface Plasmon Polaritons in Two-Dimensional Achiral Nanohole Arrays for Polarization Conversion. *Phys. Rev. B* **2017**.
- (37) Cao, Z., Ding, K., Yiu, L., Zhang, Z., Chan, C., Ong, H. Polarization Conversion of Non-Specular Diffraction Orders from Metallic Nanohole Arrays Studied by Fourier Space Polarimetry. *arxiv* **2017**.
- (38) Yiu, Y., Cao, Z., Ong, H. Strategy in Achieving Almost Complete Polarization Conversion from 2D Circular Nanohole Arrays. *CLEO Conf.* **2014**.
- (39) Cheng, Ke; Wang, Shujie; Cui, Zhonggang; Li, Qianqian; Dai, Shuxi; Du, Z. Large-Scale Fabrication of Plasmonic Gold Nanohole Arrays for Refractive Index Sensing at Visible Region. *Appl. Phys. Lett.* **2012**, 100.
- (40) Drezet, A., Genet, C., Ebbesen, T. Miniature Plasmonic Wave Plates. *Phys. Rev. Lett.* **2008**.
- (41) Gordon, R.; Sinton, D.; Kavanagh, K. L.; Brolo, A. G. A New Generation of Sensors Based on Extraordinary Optical Transmission. *Acc. Chem. Res.* **2008**.
- (42) Cao, Z., Wong, S., Wu, S., Ho, H., Ong, C. High Performing Phase-Based Surface

Plasmon Resonance Sensing from Metallic Nanohole Arrays. *Appl. Phys. Lett.* **2014**.

## Appendix A. Matlab and Lumerical FDTD Scripts

The script below is the Lumerical FDTD script used to run 41 simulations sweeping the angle of incidence from  $\theta = 0^\circ$  to  $\theta = 40^\circ$  for selected values of incident light polarization and azimuthal angle. For each simulation, the transmission in the near field and far field are saved in Matlab variables, which are then used to plot the dispersion plots.

```
1 # define 10 theta to use
2 theta = linspace(0,40,41); # (angle of incidence)
3 alpha = 0; # polarization angle of incident light
4 phi = 0;#22.5; # azimuthal angle deg; not used
5 sinphi = 0;#.38268;
6 cosphi = 1;#.92388;
7
8 # reserve matrices for p and s pol light on trans and ref monitor
9 a00b90t = matrix(length(theta),301);
10 a00b00t = matrix(length(theta),301);
11 a00b90r = matrix(length(theta),301);
12 a00b00r = matrix(length(theta),301);
13 a00trans = matrix(length(theta),151);
14 a00ref = matrix(length(theta),151);
15
16
17 # start a loop over each desired theta
18 for(i=1:length(theta)) {
19
20     # switch to layout mode so that you can edit the objects
21     switchtolayout;
22
23     # set the radius of the object named "rod" to the desired value
24     setnamed("source","angle theta",theta(i));
25     setnamed("source","polarization angle",alpha);
26
27     # overwrite previously saved data
28     #matlabsave("a90b90t",a90b90t);
29     #matlabsave("a90b00t",a90b00t);
30     #matlabsave("a90b90r",a90b90r);
31     #matlabsave("a90b00r",a90b00r);
32     matlabsave("a00trans",a00trans);
33     matlabsave("a00ref",a00ref);
34
35     # output which simulation is running
36     ?"running simulation " + num2str(i) + " of " + num2str(length(theta));
37
38     # run the simulation
39     run;
```

```

40
41 # get data from simulation
42 Ex = pinch(getdata("T", "Ex"));
43 Ey = pinch(getdata("T", "Ey"));
44 Ez = pinch(getdata("T", "Ez"));
45 RefEx = pinch(getdata("R", "Ex"));
46 RefEy = pinch(getdata("R", "Ey"));
47 RefEz = pinch(getdata("R", "Ez"));
48 MAXX = length(pinch(pinch(Ex,2,1),2,1));
49 MAXY = length(pinch(pinch(Ey,2,1),2,1));
50 freq = getdata("T", "f");
51
52 temptrans = transmission("T");
53 tempref = transmission("R");
54
55 # calc s and p pol components
56 for (f = 1:length(freq))
57 {
58     a00trans(i,f) = temptrans(f);
59     a00ref(i,f) = tempref(f);
60     for (x = 1:MAXX)
61     {
62         for(y = 1:MAXY)
63         {
64             a90b90t(i, f) = a90b90t(i, f) + abs(-Ex(x,y,f)*sinphi+Ey(x,y,f)*cosphi)^2;
65             a90b00t(i, f) = a90b00t(i, f) + abs(Ex(x,y,f)*cosphi+Ey(x,y,f)*sinphi)^2+abs(Ez(x,y,f))^2;
66             a90b90r(i, f) = a90b90r(i, f) + abs(-RefEx(x,y,f)*sinphi+RefEy(x,y,f)*cosphi)^2;
67             a90b00r(i, f) = a90b00r(i, f) + abs(RefEx(x,y,f)*cosphi+RefEy(x,y,f)*sinphi)^2+abs(RefEz(x,y,f))^2;
68         }
69     }
70 }
71 a90b90t(i, f) = a90b90t(i,f)/(MAXX*MAXY);
72 a90b00t(i, f) = a90b00t(i,f)/(MAXX*MAXY);
73 a90b90r(i, f) = a90b90r(i,f)/(MAXX*MAXY);
74 a90b00r(i, f) = a90b00r(i,f)/(MAXX*MAXY);
75 }
76 matlabsave("a00trans",a00trans);
77 matlabsave("a00ref",a00ref);
78 } # end of the main loop over the radius

```

This script takes the saved Matlab near field and far field transmission data from Lumerical FDTD simulations and generates the dispersion plots.

```

1 -   lambdapoints=151;
2 -   thetapoints=33;
3 -   lambda = [450:3:900]*10^-9; %m
4 -   hbar = 6.5821*10^-16; %eV*s
5 -   c = 2.9979*10^8; %m/s
6 -   E = 2*pi*hbar*c./lambda;
7 -   pointsize=15;
8 -   SnellFactor = 40/25.37;
9 -   k = zeros(thetapoints,lambdapoints);
10 -  for(t=1:l:thetapoints)
11 -  for(f=1:l:lambdapoints)
12 -      theta = (t-1)*2;%*SnellFactor;
13 -      k(t,f) = 2*pi/(lambda(f))*sind(theta); %1/m
14 -      k(t,f) = k(t,f)*10^-6; %(microns)^-1
15 -  end
16 -  hold on
17 -  caxis([-0.1])
18 -  scatter(k(t,1:lambdapoints),E,pointsize,-a00trans(t,1:lambdapoints),'filled');
19 -  end
20 -  xlabel('k (1/\mum)')
21 -  ylabel('Energy (eV)')
22 -  title('Near Field Transmittance with \phi=0, \alpha = 0')
23 -  axis([0 10 1.3 2.8]);|

```